Ben-Gurion University of the Negev
Faculty of Natural Sciences
Department of Physics

# Subject: IMAGING METHODS OF COLD ATOMS

Thesis submitted in partial fulfillment of the requirement for the degree of Master of Science in the Faculty of Natural Sciences.

**By: David Moravchik**

29 January, 2009

**Subject: Imaging methods of cold atoms**

**Thesis in partial fulfillment of the requirements for the degree of Master of Science**

**In the Faculty of Natural Sciences.**

**By: David Moravchik**

**Advisor: Dr. Ron Folman**

**Department of Physics**

**Faculty of Natural Sciences**

**Ben-Gurion University of the Negev**

Author's Signature: _____ Date: _____

Advisor's Signature:_____ Date: _____

Signature of the chairman of the departmental committee: _____

Date: _____

**נושא החיבור: שיטות הדמאה של אטומים קרים**

**חיבור לשם קבלת תואר "מגיסטר"**

**בפקולטה למדעי הטבע**

**מאת: דוד מורבצ'יק**

**שם המנחה: דר' רון פולמן**

**המחלקה לפיסיקה**

**הפקולטה למדעי הטבע**

**אוניברסיטת בן-גוריון בנגב**

חתימת המחבר: _____ תאריך: _____

חתימת המנחה: _____ תאריך: _____

חתימת יו"ר ועדה מחלקתית: _____ תאריך: _____

אוניברסיטת בן-גוריון בנגב
הפקולטה למדעי הטבע
המחלקה לפיסיקה

# נושא החיבור: שיטות הדמאה של אטומים קרים

**חיבור לשם קבלת תואר "מגיסטר" בפקולטה למדעי הטבע.**

**מאת: דוד מורבצ'יק**

ד' בשבט תשס"ט

29 בינואר 2009

# Abstract

Cold atoms research raises new imaging challenges for different types of experiments. Although it is possible to extract information using conventional destructive imaging techniques based upon absorption or emission, it is impossible to track the time evolution of the same atomic cloud without significantly altering its properties. Thus, it is essential, in some experiments, to use efficient non-destructive imaging in order to minimize the effect on the atoms.

Here we explore different imaging methods and characterize the differences between them to find the limits of non-destructive imaging methods under non-ideal conditions, e.g. near the atomic resonance and using large Fourier filters.

We review the fundamental concepts of atom-light interaction and diffraction theory and its implication for imaging methods using Fourier filters. In this thesis we describe our application of these methods (dark-ground and phase contrast imaging), first to dielectric samples and then to cold atomic clouds in our lab. We analyze and characterize the signals obtained by these techniques together with conventional absorption imaging.

# Acknowledgments

This work couldn't have been completed without the help of many people; first I would like to thank my advisor Dr. Ron Folman who showed me a path not only in physics but in many other fields as well. Dr. Mark Keil, your experimental skills and your scientific questions challenged me and made me wonder.

I am grateful for being given the privilege to learn from an outstanding researcher such as Dr. Yoni Japha, who taught me the meaning of being a physicist by enlightening me even when I thought that things were "sitting well" in my mind. You are my mentor and for that and many things I thank you.

I thank Dr. Plamen Petrov, for spending nights and days in the lab with me, until my experiment was complete and for your professional assistance. I also thank Shimi Machluf for making my analysis easier with an efficient data acquisition, Daniel Rohrlich for proofreading this work, the Raman team for being friends and colleagues; it was great consulting you from time to time. I was blessed to be working with students and researchers in our group that made the physics a fun world as much as an interesting one. I deeply appreciate the fabrication team, especially Dr. Yaacov Bernstein for being patient when I decided to change the wafer's thickness again and again (and again)...

I am fortunate to have the most supportive family one can wish for; non of this would have happened if I didn't have your backing.

Last but not least, I thank Gitit who had listened to my rehearsal talks over and over and supported me when I came home filled with enthusiasm and with all other emotional storms physics can do to you…

# Contents

**1 Introduction** **1**

1.1 General. . . . . 1

1.2 Overview of imaging methods . . . . . .2

1.2.1 Fluorescence imaging . . . . . 2

1.2.2 Absorption imaging . . . . . 3

1.2.3 Dark-ground imaging . . . . . 4

1.2.4 Phase contrast imaging . . . . . 5

1.3 Motivation . . . . . ..6

1.4 Thesis outline . . . . . .6

**2 Theoretical review** **7**

2.1 Basics of diffraction theory . . . . . .7

2.2 Atom-light interaction . . . . . 12

2.2.1 Multipole expansion and the dipole approximation . . . . . 12

2.2.2 Quantum picture: an atom as a dipole . . . . . .13

2.2.3 Susceptibility and refractive index . . . . . 16

2.3 Imaging atoms with a Fourier filter . . . . . .19

**3 Imaging experiments with dielectrics** **23**

3.1 Motivation. . . . . .23

3.2 Imaging system for dielectrics. . . . . 23

3.3 Phase retarding and absorbing optical elements . . . . . 25

3.4 Experimental results . . . . . .27

3.4.1 Dark-ground and phase contrast images . . . . . .27

3.4.2 Extracting the phase shift. . . . . .28

3.5 Resolution. . . . . .32

**4 Imaging techniques applied to cold atoms 35**

4.1 Imaging apparatus. . . . . .35

4.2 Image analysis . . . . . 37

4.3 Theoretical ideal signals . . . . . 44

4.4 Signal and noise analysis . . . . . 47

4.5 Derivation of atomic density. . . . . .51

**5 Summary 55**

**Appendices 57**

**A Multipole expansion 57**

**B Derivation of the polarizability 59**

**C Derivation of atom number 61**

**References 63**

# Figures


| | | |
|---|---|---|
| 1.1 | Fluorescence imaging configuration. | 3 |
| 1.2 | Absorption imaging configuration. | 3 |
| 1.3 | Dark-ground imaging configuration. | 4 |
| 1.4 | Phase contrast imaging configuration. | 5 |
| 2.1 | Light propagation through an aperture | 11 |
| 2.2 | The potential of a charge distribution | 12 |
| 2.3 | Real and imaginary parts of the susceptibility. | 18 |
| 2.4 | Phase contrast signal vs. detuning | 22 |
| 3.1 | Optical layout for imaging a dielectric sample. | 24 |
| 3.2 | Dielectric samples. | 27 |
| 3.3 | Images taken with dark-ground and phase contrast methods. | 27 |
| 3.4 | Signal vs. phase shift for dark-ground images | 29 |
| 3.5 | Signal vs. phase shift for phase contrast images | 31 |
| 3.6 | Rayleigh criterion for the resolution limit. | 33 |
| 3.7 | Intensity vs. location for dark-ground image. | 34 |
| 3.8 | Thickness measurement of ITO square. | 34 |
| 4.1 | Optical layout of cold atoms. | 36 |
| 4.2 | Retrieved absorption image. | 38 |
| 4.3 | Retrieved dark-ground image. | 39 |
| 4.4 | Fluorescence imaging of atoms in a MOT. | 40 |
| 4.5 | Phase contrast analyzed image. | 41 |
| 4.6 | Phase contrast imaging at -12MHz detuning. | 43 |
| 4.7 | Phase contrast imaging at +12MHz detuning. | 43 |
| 4.8 | Theoretical signal for absorption imaging. | 44 |
| 4.9 | Theoretical signal for dark-ground imaging. | 46 |
| 4.10 | Theoretical signal for phase contrast imaging. | 47 |
| 4.11 | Theoretical signal for non-ideal phase contrast imaging. | 47 |
| 4.12 | Dark-ground imaging signal and SNR for cold atoms. | 49 |
| 4.13 | Absorption imaging signal and SNR for cold atoms. | 51 |
| 4.14 | Comparison of dark-ground and absorption SNR. | 52 |
| 4.15 | Dark-ground - atomic density. | 53 |
| 4.16 | Absorption - atomic density. | 53 |
| A.1 | The potential of charge distribution | 57 |
| C.1 | Illustration of column density | 62 |

# תקציר

המחקר בתחום האטומים הקרים מעלה אתגרים רבים בהדמאה עבור סוגים שונים של ניסויים. למרות שניתן להשתמש בשיטות הדמאה קונבנציונאליות המבוססות על תהליכי בליעה ופליטה על מנת להפיק מידע, לא ניתן לעקוב אחרי ההתפתחות בזמן של אותו ענן אטומים מבלי לשנות את תכונותיו באופן משמעותי. לכן, בניסויים מסוימים, יש צורך במערכת הדמאה לא הרסנית ויעילה כדי למזער את ההשפעה על האטומים.

נראה בעבודה זו שיטות הדמאה שונות ונאפיין את ההבדלים ביניהן כדי למצוא את הגבולות של שיטות ההדמאה הלא-הרסניות בתנאים שאינם אידיאלים כמו בסביבת הרזוננס האטומי ובעזרת מסננים אופטיים גדולים המונחים במישור פורייה.

בעבודה זו אנו סוקרים את הבסיס התיאורטי של האינטראקציה של אור עם אטומים ומשתמשים בבסיס זה כדי לנתח ולאפיין שיטות שונות להדמאה של אטומים ובפרט שיטות המשתמשות במסננים אופטיים המונחים במישור פורייה.

בתזה מתוארות התוצאות הניסיוניות של שימוש בשיטות אלו בהדמאה של מטרות דיאלקטריות ושל אטומים קרים.

אנו מנתחים ומפרשים את התוצאות ומשווים אותן גם להדמאת הבליעה הקונבנציונלית.

# Chapter 1

# Introduction

## 1.1 General

Following the invention of the laser [Sch58] and the rapid progress of sophisticated technology during the last half-century, many scientists put their efforts into conducting experiments in which lasers are used to manipulate and monitor the time evolution of an atomic ensemble cooled to ultralow, i.e. micro-Kelvin, temperatures [Ket01, Coh97, And95, Fol02]. Almost all experimental data for ultracold atoms are obtained from optical observations [Hal03, Tur04] of a probe laser scattering from the atomic cloud. Collecting information from the scattered light exploits three processes that occur during the atom-light interaction, namely absorption, emission, and phase shift. In a two-level atomic model, absorption and scattering rates depend upon the incident light intensity (hereafter $I_0$), detuning $\delta = \omega - \omega_0$ ($\omega$ is the laser frequency and $\omega_0$ is the atomic resonance), and the excited state linewidth $\gamma$. Also, when a photon hits an atom in its ground state, it can either be absorbed or undergo a phase shift $\phi$. The atom's effect upon the photon is expressed by the complex atomic susceptibility $\chi_e$ and the complex refractive index $n$. The phase shift is related to the real part of the refractive index, which is inversely proportional to $\delta$ for large detuning, whereas absorption and fluorescence are related to the imaginary part of $n$, which falls off more rapidly with detuning far from resonance as it is inversely proportional to $\delta^2$.

Imaging capabilities based upon absorption or emission have the following disadvantage: the atoms suffer momentum kicks which may heat the atomic cloud

[Met03] and ruin the experiment. We wish instead to image the atoms with minimal effect, avoiding high absorption probabilities by keeping the probe laser frequency far from resonance. In this regime, one can image the atoms using the phase shift of the light instead of its absorbance. This technique can provide an advantage since (as mentioned above) the phase shift signal drops linearly with detuning as compared to the quadratic drop of absorption, providing higher signal-to-noise ratios and better sensitivity to atomic density. One substantial benefit of such imaging techniques is the ability to measure the time dependence of the atomic cloud, as one can measure sequential images without destroying the cloud; this non-destructive imaging also eliminates shot-to-shot fluctuations [Hal03].

## 1.2 Overview of imaging methods

The different imaging methods mentioned above have been used to extract information from the cloud; the most common extracted information is the atom number density, which can be estimated from the detected intensity via the integrated density along the light propagation direction (*"column density"*) [And97, Tur05]. Each imaging method exhibits different signal-to-noise ratios (SNR) while each technique has its own advantages and disadvantages [Tur04], as we now discuss.

### 1.2.1 Fluorescence imaging

When a laser light beam near the atomic resonance propagates through a cold atomic cloud, it will be absorbed and re-emitted. By detecting the scattered photons, we can image the cloud as illustrated in Fig. 1.1. Although this method is most convenient (as one can choose almost any imaging axis) and easy to perform, it yields a weak signal because the isotropic spatial distribution of the scattered light

results in just a small portion (in proportion to the solid angle) reaching the detector. This near-resonance imaging method, as discussed above, is destructive and may ruin the experiment.

### 1.2.2 Absorption imaging

The most common method of imaging ultracold atomic clouds is to shine a resonant probe light beam through the sample and image the "shadow" left by the atomic absorption with a camera, as depicted in Fig. 1.2. This shadow measures the spatial distribution of the cloud transmission.

Although absorption imaging yields a much higher signal-to-noise ratio than fluorescence imaging – the signal is about 100 times higher – one cannot get quantitative information for dense atomic clouds. (Since the transmission drops exponentially with atomic density, the shadow will be completely black.)

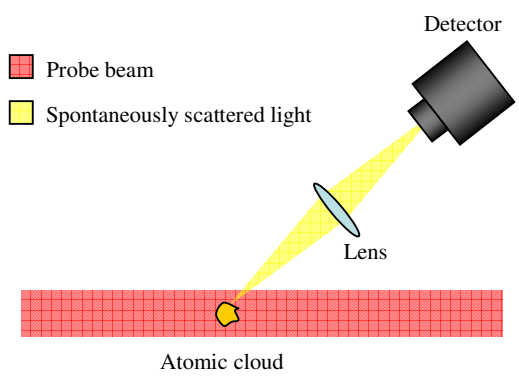


Figure 1.1 – Fluorescence imaging configuration. Some of the light is scattered by the atoms and collected by the detector to form an image of the atomic cloud.

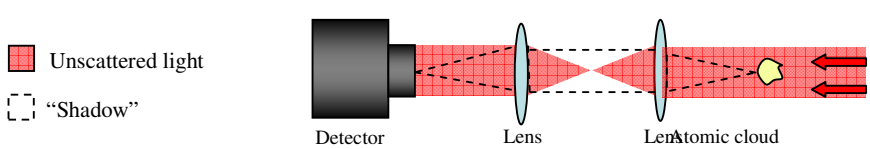


Figure 1.2 – Absorption imaging configuration. Some of the light is scattered by the atoms and the shadow created by the "missing photons" is imaged.

Allowing the atomic cloud to expand for a brief time after turning off the trap, called *time-of-flight* (TOF) imaging, can reduce the atomic density to acceptable levels, but one must then repeat the entire experiment for each flight time because of the destructiveness discussed above. Furthermore, we must bear in mind that every such repetition cannot be perfectly identical. Finally, the photon can undergo multiple scattering before emerging from optically dense clouds.

### 1.2.3 Dark-ground imaging

By placing an opaque object in the Fourier plane (the focal plane) as shown in Fig. 1.3, we block the unscattered light beam and only the scattered light will reach the detector, thus, not only the spontaneously scattered photons (as in fluorescence imaging) but also the forward scattered photons are detected, yielding a much higher signal than does fluorescence imaging. For small phase shifts, the signal received is proportional to the phase shift, $I_{DG} \propto \phi^2$, so one can determine the atomic density from the signal straightforwardly. This method does not require any analysis to retrieve the cloud, and exhibits a higher SNR than absorptive imaging methods in a far off-resonance regime.

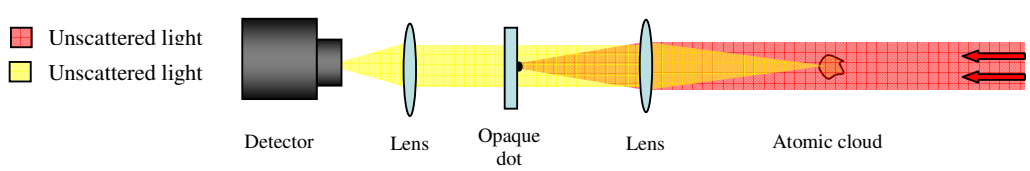


Figure 1.3 – Dark-ground imaging configuration. An opaque object at the focal point of the lens blocks the unscattered off-resonance probe beam light. By detecting the signal due to the scattered light only, we can deduce the phase shift and derive the atomic density. As the opaque dot is placed in the Fourier plane, we refer to it in this work as a Fourier filter.

### 1.2.4 Phase contrast imaging

This imaging method, first demonstrated in 1934 by Nobel Prize laureate Fritz Zernike [Zer53], is illustrated in Fig. 1.4. A probe laser beam detuned from the atomic resonance propagates through the atomic cloud, creating a phase shift in the light that is scattered, while the unscattered parallel beam is focused onto a phase shifter. The phase shifter, which is an optically flat element with a small bump or dimple in the center, adds a phase of ±π/2 (positive for a bump and negative for a dimple) only to the unscattered light and thus enhances the contrast by causing the unscattered probe light to interfere with the scattered light. The atom number density can be extracted from the detected intensity which is (as in dark-ground imaging) related to the phase shift caused by the atomic susceptibility.

For small phase shifts, the phase contrast signal is linear in the phase shift $I_{pc} \propto 1 + 2\phi$ and hence, it exhibits better SNR than the dark-ground method.

Although phase contrast imaging exhibits high sensitivity, it is not used as commonly as one would expect. The reason seems to be the difficulty in producing and aligning the required phase shifter [Mat99, Tur04, Lye03] which, depending on the size of the object, must be quite small to affect only the unscattered light.

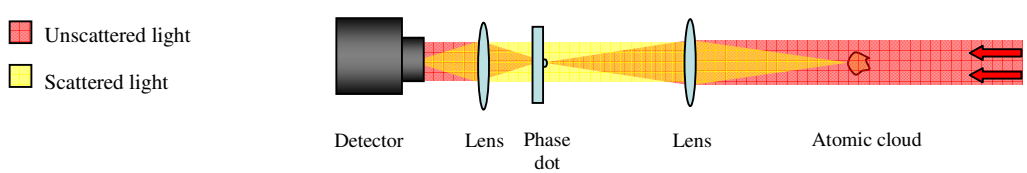


Figure 1.4 – Phase contrast imaging configuration. Off-resonant light is scattered by the atomic cloud (yellow) and interferes with the unscattered parallel beam (red). The unscattered beam is π/2 phase shifted by the phase dot. As the phase dot is placed in the Fourier plane, we refer to it in this work as a Fourier filter.

## 1.3 Motivation

As discussed above, conventional fluorescence and absorption imaging are destructive measurements which severely affect the experiment. It is essential to use a non-destructive imaging method if one desires to follow the evolution of the cloud by taking a sequence of images of the same cloud without affecting it.

In this project we discuss and experimentally demonstrate an imaging system that allows phase detection rather than conventional absorption imaging. We apply the dispersive imaging methods to cold atomic clouds in order to study signal-to-noise-ratio and resolution limitations.

Ultimately, the goal is to replace our group's absorption imaging with dispersive imaging so we could probe the evolution of cold atomic clouds. For this to happen we are required to master the world state of the art, design the required adaptation for our specific system, and perhaps even introduce improvements to the methods used so far.

## 1.4 Thesis outline

The outline of the thesis is as follows: in chapter 2 we present an overview of dispersive imaging methods by reviewing diffraction theory and the theory of atom-light interactions in a two-level atom. In chapter 3 we present results of preliminary experiments with dielectric samples made in the university's nano-fabrication center in order to characterize phase detection using a typical imaging system. Chapter 4 discusses our phase contrast, dark-ground, and absorption imaging results on cold atomic samples with our corresponding analysis of atomic densities.

# Chapter 2

# Theoretical review

In this chapter we lay the theoretical foundation for imaging of cold atoms. First, we review Fourier optics, which is the theoretical basis for manipulation of the optical phase and intensity of light. Then, we describe the interaction between light and a two-level atom when the atom is weakly excited, and derive the atomic susceptibility and the refractive index of a gas of ultracold atoms. Finally, we derive expressions for the expected signal of different imaging methods.

## 2.1 Basics of diffraction theory

One of the fascinating properties of light, *diffraction*, was experimentally reported in 1665 by Grimaldi [Goo96]. Subsequently, more than a century after Christian Huygens laid the foundation of diffraction theory, it was Augustin Jean Fresnel who predicted the light distribution upon propagation through or near an object.

Here we will present the diffraction theory for the propagation of a monochromatic light beam in a certain direction. We wish to solve the Helmholtz equation in a time-independent, linear, non-magnetic, isotropic and homogenous dielectric medium to find the electric field in a plane a distance z from an origin plane where the polarization of light is perpendicular to the plane. We start from Maxwell's equations in a homogeneous medium (MKS). [Goo96]:

$$\begin{aligned}
&\text{i.}\quad \nabla\cdot\bar{E}=0\\
&\text{ii.}\quad \nabla\cdot\bar{B}=0\\
&\text{iii.}\quad \nabla\times\bar{E}=-\frac{\partial\bar{B}}{\partial t}\\
&\text{iv.}\quad \nabla\times\bar{B}=\mu\varepsilon\frac{\partial\bar{E}}{\partial t}
\end{aligned} \tag{2.1}$$

It can be shown [Goo96, Tur04] that the *vector wave equation* can be written as

$$\nabla^2\vec{E}-\frac{n^2\left(\vec{r}\right)}{c^2}\frac{\partial^2\vec{E}}{\partial t^2}=0\,, \tag{2.2}$$

where $c$ is the light velocity in vacuum and $n$ is the refractive index defined as [Gri06]

$$n\equiv\sqrt{\frac{\varepsilon\mu}{\varepsilon_0\mu_0}}\,. \tag{2.3}$$

In our case we are interested only in one component, as our imaging beam is polarized in a plane perpendicular to the general propagation direction. Hence the vector wave equation reduces to the simpler *scalar wave equation*:

$$\nabla^2E-\frac{n^2}{c^2}\frac{\partial^2E}{\partial t^2}=0\,. \tag{2.4}$$

Let us represent a complex monochromatic plane wave as a spatially dependent amplitude $E_0\left(\vec{r}\right)$ with harmonic time dependence:

$$E\left(\vec{r},t\right)=E_0\left(\vec{r}\right)e^{-i\omega t}\,. \tag{2.5}$$

The intensity we measure is real, and defined as

$$I\left(\vec{r},t\right)=E\left(\vec{r},t\right)E^*\left(\vec{r},t\right). \tag{2.6}$$

By substituting Eq. (2.5) into Eq. (2.4) we get the Helmholz equation

$$\left(\nabla^2+k^2n^2\right)E\left(\vec{r}\right)=0\,, \tag{2.7}$$

where $k$ is the wave number:

$$k = \frac{\omega}{c} = \frac{2\pi}{\lambda}. \tag{2.8}$$

Referring to free space, the refractive index becomes unity and the free space Helmholtz equation is then

$$\left(\nabla^2 + k^2\right) E\left(\vec{r}\right) = 0. \tag{2.9}$$

We assume the following form of solution for the Helmholz equation:

$$E\left(\vec{r}\right) = E_0 e^{i\vec{k}\cdot\vec{r}} = E_0 e^{i\left(k_x x + k_y y + k_z z\right)}. \tag{2.10}$$

When substituting this form in to Eq. (2.9) we get

$$k^2 = k_x^2 + k_y^2 + k_z^2. \tag{2.11}$$

We can therefore write the solution in Eq. (2.10) as

$$E\left(x, y, z\right) = E_0 e^{i\left(k_x x + k_y y + z\sqrt{k^2 - k_x^2 - k_y^2}\right)}. \tag{2.12}$$

This solution describes a plane wave. It is clear from the exponent argument that the wave propagates infinitely as long as $k^2 > k_x^2 + k_y^2$; else, we get a rapidly decaying, z-dependent wave known as *evanescent* [Goo96] which can be neglected if we take the propagation distance to be larger than several wavelengths (as in our imaging system). Let us make use of a basic Fourier analysis and express the field at the origin plane $z = 0$ with the help of a set of simple harmonic functions and a complex amplitude $\tilde{E}\left(k_x, k_y\right)$ (a Fourier transform in the x-y plane):

$$E\left(x, y, z = 0\right) = \frac{1}{2\pi} \int \tilde{E}_{z=0}\left(k_x, k_y\right) e^{i\left(k_x x + k_y y\right)} dk_x dk_y. \tag{2.13}$$

The complex amplitude is the Fourier transform of the field at $z = 0$:

$$E_{z=0}\left(k_x, k_y\right) = \frac{1}{2\pi} \int E\left(x, y, z = 0\right) e^{-i\left(k_x x + k_y y\right)} dxdy \equiv \mathcal{F}\{E\left(x, y, z = 0\right)\}, \tag{2.14}$$

which is known as the *angular spectrum* of the wave field.

Now we propagate this field to distance z and use the plane wave traveling in different directions from the origin as derived in Eq. (2.12). We also use the linearity of the wave equation to deduce:

$$E(x, y.z) = \frac{1}{2\pi}\int \tilde{E}_{z=0}(k_x, k_y) e^{iz\sqrt{k^2-k_x^2-k_y^2}} e^{i(k_x x + k_y y)} dk_x dk_y . \qquad (2.15)$$

In many optical systems that use a beam propagating between optical elements such that the beam waist is much smaller than the distance between the elements, it is justified to use the Fresnel (or paraxial) approximation. We use the binomial expansion of $\sqrt{1+x}$ where $x$ is much smaller than unity:

$$\sqrt{1+x} = 1 + \frac{1}{2}x + \ldots . \qquad (2.16)$$

Applying Eq. (2.16) to Eq. (2.15) yields

$$\sqrt{k - k_x^2 - k_y^2} \sim k\left(1 - \frac{k_x^2}{2k^2} - \frac{k_y^2}{2k^2}\right). \qquad (2.17)$$

Therefore,

$$E(x, y, z) = e^{ikz}\int dk_x dk_y e^{i(k_x x + k_y y)} \tilde{E}_{z=0}(k_x, k_y) e^{\frac{-iz}{2k}(k_x^2 + k_y^2)}, \qquad (2.18)$$

where the phase factor $e^{ikz}$, which does not depends on the transverse coordinates, is later ignored. Using the convolution theorem we derive

$$E(x, y, z) = \frac{1}{i\lambda z}\int dx'dy' E(x', y', z=0) e^{-\frac{i\pi}{\lambda z}\left((x-x')^2 + (y-y')^2\right)} . \qquad (2.19)$$

Eq. (2.19) is the Fresnel diffraction formula, which is commonly used to describe beam propagation in free space. Now we show that the field at very large distance (in the far field limit) reveals the angular spectrum (Fourier transform) of the beam at the origin. By expanding the quadratic arguments of the exponent in Eq. (2.19) we obtain

$$E(x, y, z) = \frac{1}{z\lambda i} e^{ikz} e^{\frac{ik}{2z}(x^2+y^2)} \int E(x', y', z=0) e^{\frac{ik}{2z}(x'^2+y'^2)} e^{-\frac{ik}{z}(xx'+yy')} dx'dy' . \qquad (2.20)$$

When z is much larger than the width of the beam at $z=0$, the terms $x'^2/z$ and $y'^2/z$ vanish, while $x/z=\tan(\theta)\cos(\phi)$ and $y/z=\tan(\theta)\sin(\phi)$ stay constant and represent the angle of propagation as demonstrated in Fig. 2.1. The integral in Eq. (2.20) is then the *Fourier transform* $\mathcal{F}$ of the complex electric field at the origin plane, with an additional quadratic phase representing a spherical wave front. Equation (2.20) can be written as:

$$E(f_x, f_y) = \frac{1}{z\lambda i} e^{ikz} e^{\frac{ik}{2z}\left(f_x^2+f_y^2\right)} \mathcal{F}\left\{E(x', y', z=0)\right\}, \tag{2.21}$$

where here we define $f_x, f_y$ as the *spatial frequencies*

$$\begin{aligned} f_x &= \frac{kx}{z}, \\ f_y &= \frac{ky}{z}. \end{aligned} \tag{2.22}$$

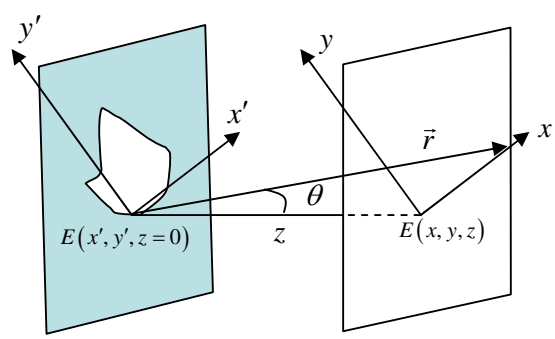


Figure 2.1 – Light propagation through an aperture.

## 2.2 Atom-light interaction

Let us derive an expression for the complex refractive index of a cold atomic cloud, starting from a microscopic view of a single atom and arriving at a macroscopic expansion for a dilute gas. We start from the general concept of dipole distribution and then present the quantum theory of light-matter interaction in the weak coupling limit.

### 2.2.1 Multipole expansion and the dipole approximation

The electrostatic potential of an arbitrary charge distribution $\rho(\vec{r})$ at a point R is as follows [Gri99]:

$$V(\vec{R}) = \frac{1}{4\pi\varepsilon_0}\int \frac{1}{|\vec{R}-\vec{r}|}\rho(\vec{r})\,d\tau\,, \tag{2.23}$$

where $\rho(\vec{r})d\tau$ is an infinitesimal charge element as illustrated in Fig. 2.2. When the point of observation $R$ is well outside the charge distribution, Eq. (2.23) is reduced (cf. Appendix A) as follows: we can simplify it with a unit vector $\hat{R}$:

$$V(\vec{R}) = \frac{1}{4\pi\varepsilon_0}\frac{\hat{R}\cdot\vec{d}}{R^2}\,, \tag{2.24}$$

where the *dipole moment* $\vec{d}$ of the charge distribution $\rho(\vec{r})$ is defined as

$$\vec{d} \equiv \int \vec{r}\rho(\vec{r})\,d\tau\,. \tag{2.25}$$

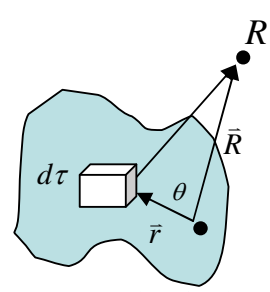


Figure 2.2 – The potential of a charge distribution.

Therefore, if we look at a classical dipole of two opposite charges $\pm q$ separated by a distance $\vec{r}$, we get:

$$\vec{d} = q\vec{r}\,. \tag{2.26}$$

When a bound charge is introduced into an electric field, it redistributes, and a dipole moment is induced in the medium. An atom is said to be *polarized* when its total dipole moment is not zero. The relation between the induced dipole moment in any specific species of atom or molecule is given by [Goo96]

$$\vec{d} = \alpha \vec{E}\,, \tag{2.27}$$

where $\alpha$ is the polarizability.

### 2.2.2 Quantum picture: an atom as a dipole

Classically, a single atom in a weak electric field can be viewed as an driven oscillator with a damping force of $\gamma$. In the case where the light field is relatively close to resonance with a single atomic level, we can look at the atom as a two-level system with a ground and a single excited state.

Let $|g\rangle$ and $|e\rangle$ be the ground and excited energy levels of a two-level atom with an electron wave function which is a superposition of eigenstates $\psi_g(\vec{r})$, $\psi_e(\vec{r})$. Then, a general state of the atom is given by [Met03]

$$|\psi\rangle = a|\psi_g\rangle + b|\psi_e\rangle \equiv \begin{pmatrix} a \\ b \end{pmatrix}, \tag{2.28}$$

where $|a|^2$ and $|b|^2$ are the probabilities of the electron to be found in each level. Using the electron wave function we can determine the probability density $p(\vec{r})$ to find a charge at a spatial region:

$$p(\vec{r}) = |\psi(\vec{r})|^2\,. \tag{2.29}$$

Clearly,

$$\int p(\vec{r})\,d\vec{r} = \int \left|\psi(\vec{r})\right|^2 d\vec{r} = |a|^2 + |b|^2 = 1. \tag{2.30}$$

For a neutral atom with zero total charge, we sum over all charge distribution $p_{tot}(\vec{r})$ to get zero:

$$\int p_{tot}(\vec{r})\,d\vec{r} = 0. \tag{2.31}$$

We wish to find an expression for the atomic dipole moment in order to find the susceptibility. Therefore we use the definition of an electric dipole far enough from observation point [Gri99] and define a dipole operator $\hat{\vec{d}} = e\hat{\vec{r}}$ with the expectation value:

$$\left\langle \hat{\vec{d}} \right\rangle = \int e\vec{r}p(\vec{r})\,d\vec{r}, \tag{2.32}$$

where $e$ is the electron charge. Substituting Eq. (2.29) into Eq. (2.32), we find the expectation value of the dipole in a two-level atom:

$$\left\langle \hat{\vec{d}} \right\rangle = \int e\vec{r}\left|\psi(\vec{r})\right|^2 d\vec{r}. \tag{2.33}$$

Substituting Eq. (2.28) into Eq. (2.33) and bearing in mind that integration over all space of anti-symmetric functions eliminates Eq. (2.33) may be reduced as follows: we choose the quantization axis of the atom to be aligned with the direction of the dipole moment such that we may replace the dipole operator with a scalar:

$$\left\langle \hat{d} \right\rangle = a^* b d_{ge} + a b^* d_{eg}, \tag{2.34}$$

where $d_{ge} = d_{eg}^*$ is the matrix element of the dipole operator between the two levels:

$$d_{ge} = e\int d\vec{r}\,\hat{n}\cdot\vec{r}\psi_g^*(\vec{r})\psi_e(\vec{r}) \equiv \left\langle \psi_g \left| \hat{d} \right| \psi_e \right\rangle, \tag{2.35}$$

in which $\hat{n}$ is a unit vector in the quantization axis direction.

The free non-interacting Hamiltonian of an atom can be written as [Lou83]

$$\hat{\mathcal{H}}_A = E_g \left| g \right\rangle \left\langle g \right| + E_e \left| e \right\rangle \left\langle e \right| = \begin{pmatrix} E_g & 0 \\ 0 & E_e \end{pmatrix}, \tag{2.36}$$

where $E_e - E_g = \hbar\omega_0$ and $\omega_0$ is the atomic transition frequency. Hence,

$$\hat{\mathcal{H}}_A \left| \psi \right\rangle = aE_g \left| g \right\rangle + bE_e \left| e \right\rangle . \tag{2.37}$$

We now add a weak interacting field equivalent to a driving field $\vec{E}$ acting on the free oscillator:

$$\vec{E} = \vec{E}_0 \cos \omega t . \tag{2.38}$$

The Hamiltonian of the atom-field interaction is

$$\hat{\mathcal{H}}_{AF} = -\vec{d} \cdot \vec{E} . \tag{2.39}$$

Now we choose the quantization axis of the atom to be aligned with the direction of the field (for linearly polarized light), such that we may replace the dipole operator and the field with scalars. We can therefore write the atom-field Hamiltonian as

$$\hat{\mathcal{H}}_{AF} = \begin{pmatrix} 0 & -d_{ge} \\ -d_{eg} & 0 \end{pmatrix} E_0 \cos\left(\omega t\right). \tag{2.40}$$

We now neglect counter-rotating terms, i.e. we apply the *rotating wave approximation* (RWA) [Lou83]:

$$\hat{\mathcal{H}}_{AF} = \begin{pmatrix} 0 & -d_{ge} e^{i\omega t} \\ -d_{eg} e^{-i\omega t} & 0 \end{pmatrix} E_0 . \tag{2.41}$$

Now we wish to write the total Hamiltonian $\hat{\mathcal{H}}$ of the atom and atom-field interaction:

$$\hat{\mathcal{H}} = \hat{\mathcal{H}}_A + \hat{\mathcal{H}}_{AF} = \begin{pmatrix} E_g & -d_{ge} e^{i\omega t} \\ -d_{eg} e^{-i\omega t} & E_e \end{pmatrix}; \tag{2.42}$$

we apply $\hat{\mathcal{H}}$ to the electron wave function and use Schrödinger equation:

$$i\hbar \frac{d}{dt}\begin{pmatrix} a(t) \\ b(t) \end{pmatrix} = \hat{\mathcal{H}}\begin{pmatrix} a(t) \\ b(t) \end{pmatrix}. \tag{2.43}$$

A steady-state solution of the Schrödinger equation with additional damping rate $\gamma/2$ from the excited state to the ground state leads to the following (Appendix B):

$$\left\langle \hat{d}(t) \right\rangle = -\frac{|d|^2 E(t)/\hbar}{\delta + i\gamma/2} + c.c\,,$$

where $\delta \equiv \omega - \omega_0$ is the detuning from atomic resonance. It follows that the polarizability of an atom in an electric field is given by

$$\alpha = -\frac{|d_{ge}|^2}{\hbar}\frac{1}{\delta + i\gamma/2}. \tag{2.44}$$

### 2.2.3 Susceptibility and refractive index

We now expand our discussion to the macroscopic scale where the light beam is transmitted through a volume with many atoms, which can be considered as a dielectric medium. We define the *polarization* $\vec{P}(\vec{r},t)$ as the amount of dipole moment per unit volume $d\tau$, which is, basically, how many small dipoles exist per volume and how much they are induced by the electric field. Hence:

$$\vec{P}(\vec{r},t) = n_{dipoles}\left\langle \hat{d} \right\rangle \tag{2.45}$$

where $\left\langle \hat{d} \right\rangle$ is the dipole moment of a single dipole and $n_{dipoles}$ is the number of dipoles. On the other hand, the macroscopic linear response of the polarization to the field, analogous to the microscopic equation Eq. (2.27), is given by

$$\vec{P}(\vec{r},t) = \varepsilon_0 \chi_e \vec{E}(\vec{r},t). \tag{2.46}$$

Here we defined the proportionality constant $\chi_e$ as the *electric susceptibility*. Thus, using Eq. (2.44), we get

$$\chi_e = \frac{n_{atoms}\alpha}{\varepsilon_0} = -\frac{n_{atoms}(\vec{r})}{\varepsilon_0}\frac{|d_{ge}|^2}{\hbar}\frac{\delta - i\gamma/2}{\delta^2 + (\gamma/2)^2}. \tag{2.47}$$

Let us now look at the plane-wave solution to the wave equation for a homogeneous isotropic dielectric medium:

$$\tilde{E}(z,t) = \tilde{E}_0 e^{i(kz-\omega t)}. \tag{2.48}$$

Here we have defined a complex wave number:

$$k = n\frac{\omega}{c}, \tag{2.49}$$

where the refractive index $n$ is defined as [Tur04]:

$$n = \sqrt{\varepsilon_r} = \sqrt{1+\chi_e}. \tag{2.50}$$

When the susceptibility is small relative to 1 we can use a binomial approximation for the square root, such that

$$n \sim 1 + \frac{1}{2}\chi_e. \tag{2.51}$$

Thus, the optical properties of the atomic cloud are governed by the real and imaginary parts of the susceptibility. The absorption is governed by the real part of the susceptibility and the phase shift is governed by the imaginary part of the susceptibility, as follows:

Let $E_0$ be the field at the plane preceding the cloud; then, after propagating in the cloud in the z direction, the field $E$ is attenuated and phase shifted as follows [Ket99]:

$$E = E_0 t e^{i\phi}, \tag{2.52}$$

where $t$ is the transmission, corresponding to the real part of the susceptibility, and $\phi$ is the phase shift, corresponding to the imaginary part, as follows [Ket99, Tur04, Cha97]:

$$t = e^{-\kappa} = e^{-\frac{OD}{2}\frac{1}{1+\Delta^2}} \tag{2.53}$$

$$\phi = -\frac{OD}{2}\frac{\Delta}{1+\Delta^2} \tag{2.54}$$

where $\Delta = \frac{\delta}{\gamma/2}$ is the detuning in half line widths, $OD$ is the optical density defined as the product of the *column density* $\tilde{n}$ with the resonant absorption cross-section $\sigma_0$:

$$OD = \sigma_0 \tilde{n}\,, \tag{2.55}$$

in which [Ket99]

$$\sigma_0 = \frac{3\lambda^2}{2\pi}\,, \tag{2.56}$$

and $\tilde{n}$ is defined as the projection of the density along the $z$ axis (see Appendix Fig. C.1):

$$\tilde{n} = \int_z n_{atoms}\, dz\,. \tag{2.57}$$

From this measured column density we wish to extract the number of atoms in our atomic clouds.

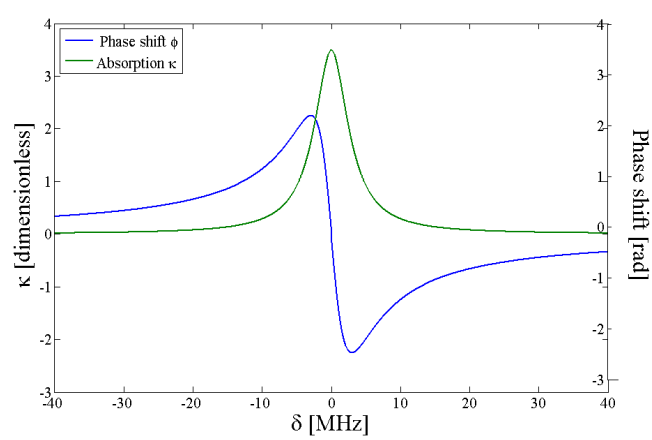


Figure 2.3 – Absorption $\kappa$ and phase shift $\phi$ as a function of detuning $\delta$ for an optical density of 7 for $^{87}$Rb with linewidth of γ=6 MHz.

## 2.3 Imaging atoms with a Fourier filter

Let us derive an expression for the imaging signal for a few of the imaging systems described in section 1.2. The light beam at the object plane (right after the object) is Fourier transformed by a first lens into the Fourier plane (at its focal plane). Next, a Fourier filter placed at the Fourier plane may either block (in dark-ground imaging) or phase-shift (in phase-contrast imaging) a part of the incident light beam. Then, a second lens performs an inverse Fourier transform into the image plane (the plane of the camera). Here we obtain the theoretical form of this signal.

Let $E_0$ be a collimated ingoing light beam. We define the object plane at $z_0$ as the plane perpendicular to the beam, which is located just after the beam has passed through the object. If the object is optically thin (i.e. the beam is not severely distorted while passing through the object), then the field in the object plane is given by

$$E(x, y, z_0) = E_0 t(x, y) e^{i\phi(x,y)}, \tag{2.58}$$

where $\phi(x, y)$ is the phase shift as determined by the real part of the complex refractive index and $t(x, y)$ is the transmission determined by the imaginary part of the complex refractive index as in Eq. (2.54) and Eq. (2.53) follows.

At the back focal plane (i.e. the *Fourier plane* denoted by $z_f$) of the first imaging lens, we apply Eq. (2.21) to derive the field:

$$E(x_f, y_f, z_f) = \frac{1}{i\lambda f} \int E(x', y', z_0) e^{-i\frac{2\pi x}{\lambda f}x'} e^{-i\frac{2\pi y}{\lambda f}y'} dx'dy', \tag{2.59}$$

where $f$ is the focal length and $z_0$ is the plane where $z = 0$.

An arbitrary Fourier filter (i.e. an object placed at the back focal plane of the first imaging lens) may be represented by a region $R(x,y)$ (1 when $x,y$ is within the region and 0 elsewhere), where the light beam is transmitted with an amplitude $\tau$ and an additional phase $\theta$ is imparted. For dark-ground imaging we set $\tau=0$ (no transmission through the opaque region), while for phase contrast imaging $\tau=1$ and $\theta=\pi/2$. The shape of the region $R(x,y)$ is usually designed such that the unscattered light from the main beam falls within the region, while the light scattered from the object falls outside the region $R(x,y)$. The field at the image plane $z_i$ (i.e. at the focal point of a second imaging lens) would be represented by another Fourier transform as follows:

$$E(x,y,z_i)=\frac{1}{i\lambda f}\int\left\{\tau R(x',y')e^{i\theta}+\left[1-R(x',y')\right]\right\}E(x',y',z_f)e^{-i\frac{2\pi x'}{\lambda f}x}e^{-i\frac{2\pi y'}{\lambda f}y}dx'dy', \quad (2.60)$$

where for simplicity we have assumed that the focal length of the second lens is similar to that of the first (magnification *M=1*). As $E(x,y,z_f)$ itself is a Fourier transform of the field $E(x,y,0)$ at the object plane, we may use the convolution theorem to write the field at the image plane as a convolution of the field in the object plane and the Fourier transform of the expression in the curly brackets:

$$\begin{aligned}E(x,y,z_i)=\int\Big\{&\tau r(x-x',y-y')e^{i\theta}+\left[\delta(x-x')\delta(y-y')-r(x-x',y-y')\right]\Big\}\\&\cdot E(x',y',z_0)dx'dy'\end{aligned} \quad (2.61)$$

where $r(x,y)$ is a Fourier transform of the range $R(x',y')$:

$$r(x,y)=\frac{1}{i\lambda f}\int R(x',y')e^{-i2\pi xx'/\lambda f}e^{-i2\pi yy'/\lambda f}dx'dy'. \quad (2.62)$$

By using Eq. (2.58) we obtain

$$E(x,y,z_i)=E_0\left[t(x,y)e^{i\phi(x,y)}+s(x,y)e^{i\alpha}\left(\tau e^{i\theta}-1\right)\right], \quad (2.63)$$

where we have defined

$$s(x,y)e^{i\alpha(x,y)} \equiv \int dx'dy' r(x-x', y-y') t(x', y') e^{i\phi(x',y')}. \tag{2.64}$$

In the limit where the range $R(x,y)$ of the Fourier filter is very small compared to the Fourier image of the object, its Fourier transform $r(x,y)$ is much broader than the region where the transmission $t(x,y)$ is smaller than 1. It follows that in this ideal limit where only the unscattered light falls on the region $R$, we can replace $s$ by 1.

To be consistent with most literature [Sal07, Tur04] the optical intensity will be defined as

$$I(\vec{r}) = \left|E(\vec{r})\right|^2. \tag{2.65}$$

Keeping in mind that we are interested in ratios between intensities this is an adequate definition. Thus, in the image plane we find the intensity as follows:

$$I(x,y,z_i) = I_0\left\{t^2 + s^2\left(1+\tau^2 - 2\tau\cos\theta\right) + 2st\left(\tau\cos\left(\theta+\alpha-\phi\right) - \cos\left(\alpha-\phi\right)\right)\right\}, \tag{2.66}$$

where $I_0 = \left|E_0\right|^2$. Indeed, for different imaging methods we find different intensities. If no spatial filter is placed at the Fourier plane i.e. $\theta = 0$, $\tau = 1$, we derive the known Beer-Lambert law:

$$I(x,y,z_i) = t^2 I_0. \tag{2.67}$$

For dark-ground, the theoretical optimal signal is obtained when $\tau = 0$, $s = 1$, and $\alpha = 1$:

$$I(x,y,z_i) = I_0\left\{t^2 + 1 - 2t\cos\left(\phi\right)\right\}. \tag{2.68}$$

Thus, for sufficiently small phase shifts, i.e. $\phi << 1$, one can make the following approximation:

$$I\left(x,y,z_i\right)=I_0\left[\left(1-t\right)^2+t\phi^2\right]. \tag{2.69}$$

Most worldwide experiments have been conducted at large detuning such that the transmission can be approximated to unity: $t\sim 1$. One then finds the dark-ground signal at far off-resonance to have the simple quadratic form:

$$I\left(x,y,z_i\right)\sim I_0\phi^2. \tag{2.70}$$

Finally we refer to the phase-contrast imaging method to find the theoretical expected signal. For ideal imaging we set $s=1$ , $\alpha=0$, $\theta=\pi/2$ and $\tau=1$, and we find the phase-contrast intensity:

$$I\left(x,y,z_i\right)=I_0\left\{2+t^2-2\sqrt{2}t\cos\left(\phi+\frac{\pi}{4}\right)\right\}. \tag{2.71}$$

The phase-contrast signal for small phase shifts and far detuning $t\sim 1$ is derived using a Taylor expansion:

$$I=I_0\left(1+2\phi\right). \tag{2.72}$$

In the following chapters we will make use of these expressions as we are analyzing the signal received via the different imaging methods. In particular we use a non-ideal Fourier filter which retards the phase by $\pi/2.5$. This will not extremely affect the signal, but slightly reduces it, as can be seen in Fig. 2.4.

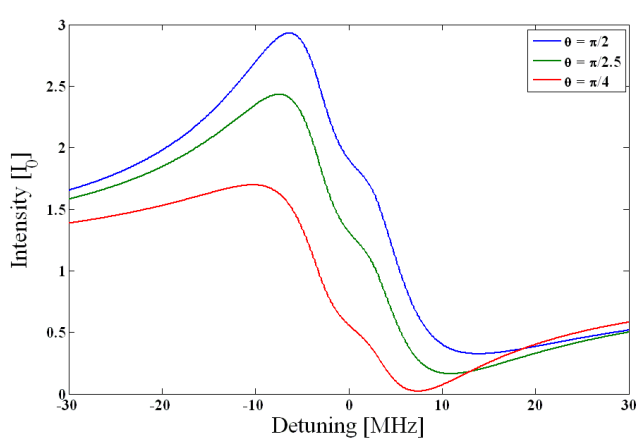


Figure 2.4 – Phase contrast signal versus detuning for a fixed optical density of 6. A peak signal is at $\theta=\pi/2$.

# Chapter 3

# Imaging experiments with dielectrics

## 3.1 Motivation

We wish to have a clear and sharp image of a cold atomic cloud in order to extract information regarding its size and shape. To that end, we must construct an imaging system that allows size and shape extraction.

In this chapter we will identify our imaging limitations by examining capabilities in terms of resolution and phase-shift detection. We analyze the results of preliminary imaging experiments with dielectric samples.

We will attempt to imitate the actual cold atomic-cloud system by placing a target which retards the phase of the incoming probe light beam at the object plane, and we image it to obtain a better understanding of our sensitivity and resolution limits.

## 3.2 Imaging system for dielectrics

Different imaging techniques demands different setups. We present the basic imaging layout in Fig. 3.1. For this preliminary stage, it is most convenient to use a visible Helium-Neon (HeNe) laser with a wavelength of 633 nm as a probe so as to simplify alignment. We attenuate the laser intensity, to prevent camera saturation, with a neutral density filter (each time with different transmission), and we use 75 mm and 300 mm focal-length lenses in a telescope configuration setup in order to expand the beam's waist radius to 4 mm so as to cover the entire object.

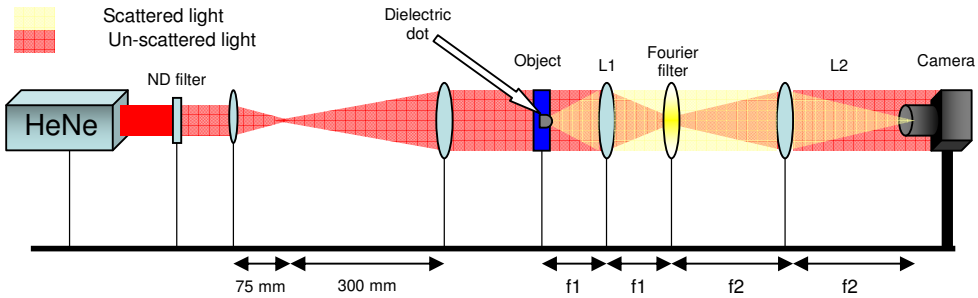


Figure 3.1 – Optical layout for imaging dielectric samples. The HeNe laser probe beam is attenuated by a neutral density filter (ND) and expanded by a telescope. The probe passes through a phase-retarding object (simulating atoms) at the focal point of lens L1 and the beam is now composed of an undisturbed component i.e. unscattered light (in red) and a second component which is the change due to an object i.e. the scattered light (in yellow). At the back focal plane of L1 lens we used a Fourier filter to block (for dark-ground) or phase-shift (for phase contrast) the unscattered light. In more accurate language one may say that the low spatial frequency components of the image pass through the Fourier filter while the high spatial frequency components do not. The second lens (L2) reconstructs the image of the filtered Fourier transform on the camera.

After the object plane, the collimated beam passed through two additional lenses with f1=200 mm, f2=100 mm (ThorLabs AC-508) with a Fourier filter between them at the Fourier plane. These lenses were chosen to simulate the actual distance from the atomic cloud to our first imaging lens; we cannot approach the cloud because of the distance between it and the vacuum chamber window (about 200 mm). In addition, we could not use lenses with large focal length, as available space on the optical table was limited; for this reason f2 was chosen to be 100 mm, creating a demagnification of 2. We used a camera with a pixel size of 6 μm × 6 μm (IDS uEye-1220M) as this is a compact low-cost camera which will be used later to image the cold atoms.

Our Fourier filter was changed according to the imaging method. For dark-ground we used a chromium disc with a 200 μm diameter. For phase contrast we used a 200 μm Indium Tin Oxide (ITO) disc. These specifications were not chosen arbitrarily – they correspond to the central width of the diffraction pattern size of a typical object.

## 3.3 Phase-retarding and -absorbing optical elements

In order to simulate the imaging of cold atomic clouds we have to create a phase-retarding sample of the size of our cloud, with weak absorbance. To do so, we manufactured (in the University's fabrication facility) a dielectric sample as follows:

We used a 3" borosilicate glass wafer, 0.5 mm thick, covered with a thin layer of variably shaped ITO (see below). We used ITO for its low absorbance (~15% at 633 nm for all our samples) and its common use in the fabrication center. Its refractive index is typically in the range of 1.8 to 2.3 [Swa83]; we conducted an independent ellipsometer measurement and found its refractive index to be 2.13. The shapes we chose were circles, squares and rectangles with 3:1 aspect ratio. All shapes were fabricated in three rows and with a 1 mm headline of 'BGU PCI' to show the wafer's orientation. The circles' diameters, squares' sides, and the longitudinal edges of the rectangles were set from 200 μm to 3 μm as shown in Fig. 3.2. These dimensions were determined by the following considerations: the smallest feature shouldn't be smaller than the spot size of the probe laser beam in the focal plane, because we have to ensure that the unscattered light will be completely filtered. Moreover, the maximal reasonable size was determined according to an analytic estimation of the expected Fourier transform image of an atomic cloud of 100 μm in the Fourier plane i.e. at the back focal plane of the objective L1. One can find the width of the diffraction pattern of a Gaussian intensity distribution (at 1/e) $\Delta x'$ as follows [Sal07]:

$$\Delta x' = \frac{2 f_1 \lambda}{\pi \Delta x}. \tag{3.1}$$

For a 100 μm diameter cloud using an imaging lens of focal length $f_1$=200 mm, and the HeNe laser, one finds $\Delta x'$ to be ~800 μm. For a lens with a focal length of 300

mm and with our diode laser at 780 nm one finds $\Delta x'$ to be roughly 1.5 mm. It follows that a phase dot or opaque dot of 200 μm or less will successfully transmit most of the spectral features of the atomic cloud undisturbed. On the other hand, our probe spot size is 8 mm. This implies that the spot size at the center of the Fourier plane is 10 μm. Hence, it is expected that for dots with a diameter of more than 10 μm, all of the unscattered light will be blocked or phase shifted.

Transparent micrometric features are difficult to align; it is also hard to distinguish an ITO feature from other elements on the wafer (such as dust). However, the spacing between all features in a row is constant (6.9 mm), allowing easy swapping between the features so long as one measures the translation. Furthermore, although ITO is almost transparent to visible light, its reflection (less than 15%) can be detected, indicating that the dot is centered. We made four wafers with different ITO thicknesses, 35 nm, 88 nm, 137 nm and 314 nm, to apply different phase shifts. An additional wafer was made with a chromium layer of 320 nm to absorb the unscattered light when conducting dark-ground imaging experiments. The wafers vary in their thicknesses (denoted by $t$); they apply different phase shifts $\phi$ to the probe beam according to [Hal03]:

$$\phi = \frac{2\pi(n-1)t}{\lambda}, \tag{3.2}$$

where $n$ is the refractive index and $\lambda$ is the wavelength in vacuum. Thus, for 35 nm, 88 nm, 137 nm and 314 nm layers we get phase shifts of about $\pi/8$, $\pi/3$, $\pi/2$, $\pi$ respectively. All wafers were used as objects, with the 137 nm thick layer wafer being used solely as a Fourier filter on the phase-contrast imaging configuration.

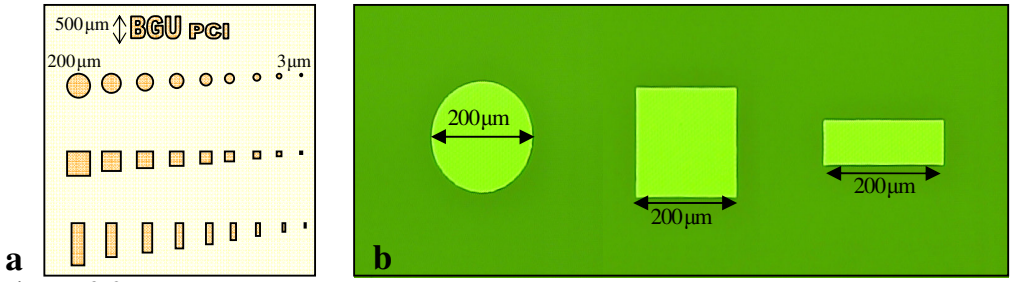


Figure 3.2 – (a) ITO features on a 3" glass wafer. Circles, squares and rectangles are sequentially ordered by their size. (b) Here, a 200 µm circle, square and rectangle imaged with a dark field microscope. These structures were used both for the object and for the phase dot.

## 3.4 Experimental results

### 3.4.1 Dark-ground and phase contrast images

Initially, we imaged a 314 nm thick ITO sample since it applies a sufficiently high phase shift, i.e. strong and easy detectable signal. Dark-ground and phase contrast images were taken (Fig. 3.3) using the same optical layout shown on Fig. 3.1, changing the Fourier filter according to the imaging method and exchanging between L1 and L2 to study different magnifications.

Fourier filtering demands high precision when dealing with diffraction patterns ($\Delta x'$ of the order of 100 µm), and for that reason we used a micrometric translation stage to change the filter's location.

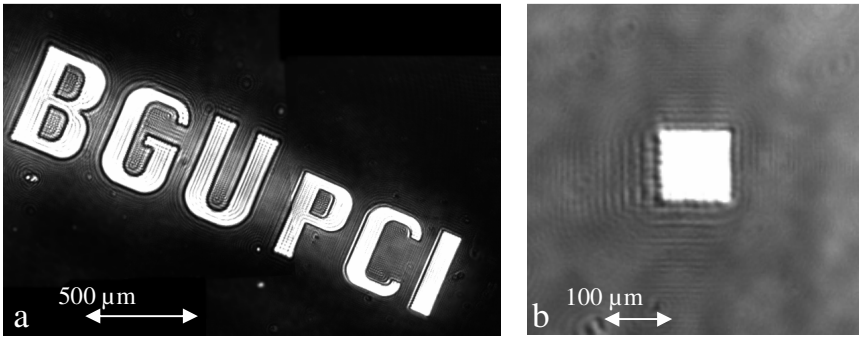


Figure 3.3 – (a) Dark-ground image of a magnified (f1=100 mm, f2=200 mm) ITO wafer's headline. Here we used a 200 µm chromium disk as a Fourier filter. (b) Phase contrast image of 100 µm magnified square (f1=100 mm, f2=200 mm). The square's thickness is 314 nm and the Fourier filter is a 200 µm disc of 137 nm thick ITO. For both images a 150 µW probe power was used and the camera's exposure time was 214 µs.

### 3.4.2 Extracting the phase shift

We used our optical setup with f1=100 mm and f2=200 mm to image ITO features with different intensities and different thicknesses. With each picture taken, we chose a 20 × 20 pixels sub-matrix at the center of the object with its mean pixel value to be our signal $\langle S \rangle$. The size of the sub-matrix cannot exceed the dimensions of the object but must be big enough for its mean value to approximate the real intensity.

For a Gaussian intensity profile one would expect higher signal at the center of the beam rather than at the edges (because $I \propto I_0$). But in our case, one can neglect the intensity variation in $I_0$ because the imaging beam waist radius is 4 mm; thus, when it propagates through the region of interest (which is an order of magnitude smaller) the intensity is approximately constant. Moreover, the object is flat; having a uniform signal that can be measured with good accuracy by a 20-pixel matrix.

Let us find the camera's pixel readout in terms of laser intensity in order to estimate the signal in terms of power. The overall readout of all pixels of a completely covered camera is $2.9 \times 10^4$. (This total readout is regarded as noise). We now shine a laser beam into the camera and calculate the total pixel readout (about $\sim 51 \times 10^6$ for 130 μW and $\sim 58 \times 10^6$ for 150 μW with an exposure time of 214 μs); we ensure the beam is completely overlapped by the camera and that the intensity is low enough to avoid camera saturation. The change in the overall detected pixel readout is then equivalent to the total incoming beam's intensity as follows:

$$\frac{\text{Total power}}{\text{The difference in pixel's total readout}} = \text{Power per pixel readout}$$

$$\frac{130\ \mu\text{W}}{51\times10^{6} - 2.9\times10^{4}} \sim 2.5\ \frac{\text{pW}}{\text{Single pixel's readout}} \tag{3.3}$$

As confirmation, for an imaging beam of 150 μW we find the same intensity per pixel readout. If one wishes to conduct an independent measurement (with different settings as longer exposure time), one can find the number of photon per pixel at a single pixel readout as follows:

$$\frac{\text{Power per pixel readout}}{\text{Single photon's energy}} \times \left(\text{Exposure time}\right) \sim 1700 \text{ Photons per pixel}. \tag{3.4}$$

In order to find the relation between phase shift and detected signal, we used fixed probe intensity with the same dark-ground and phase contrast optical layouts (f1=100 mm, f2=200 mm, 200 μm opaque and ITO discs as Fourier filters for dark-ground and phase contrast respectively) while changing the object's thickness.

Fig. 3.4 shows the measured values of the average pixel readout against a fit to

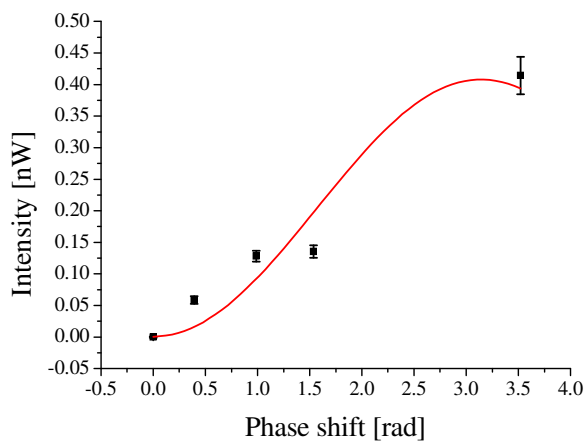


Figure 3.4 – Signal of dark-ground images $<S>$ for magnified 200 μm ITO squares with different thicknesses: 35 nm, 88 nm, 137 nm, 314 nm. The probe's constant power was 84 μW, which is low enough to avoid camera saturation. The error-bars are the standard deviation of the 20x20 pixel matrix around its mean value $<S>$. Red curve denotes the fit according to Eq. (2.68) with transmission of $t^2 = 0.85$

the theoretical function according to Eq. (2.68) with transmission of $t^2 = 0.85$ (as was measured for the ITO samples). The fitting parameter $I_0$ is found to be $I_0 = 45$ pixel readouts (with an error of ~10%). Thus, the incoming intensity $I_0$ in nW per pixel is:

$$45 \times 0.0025 \ \frac{nW}{\text{Single pixel's readout}} = 0.11 \ \frac{nW}{\text{pixel}} \tag{3.5}$$

Let us now use the known incoming beam power to derive the expected intensity per pixel in an ideal system where all the light scattered from the object reaches the camera. The imaging beam has a total power of $P = 84$ μW therefore the intensity per pixel is

$$I_{0\ \text{per pixel}} = \frac{2P}{W_0^2 \pi} \times \text{pixel area} = \frac{2 \cdot 84\ \mu\text{W}}{\left(4 \times 10^{-3}\right)^2 \pi} \times 36 \times 10^{-12} \sim 0.12 \ \frac{\text{nW}}{\text{pixel}}, \tag{3.6}$$

where $W_0$ is the beam waist radius in meters. The intensity per pixel as calculated by the measured ingoing power is ~10% larger, but remains in the error range. Presumably, the filtered unscattered light and the intensity loss during propagation through the optics reduced the beam power detected by the camera. However, the main cause of the reduction in intensity may be the blocking of some low spatial frequency components of the light scattered from the object by the opaque dot.

The same measurement was done using the phase-contrast technique but only three wafers were imaged as one (137 nm thick) was used as a Fourier filter. Fig. 3.5 shows the measured values versus phase with a fit to the theoretical function of phase-contrast signal - Eq. (2.66) with $s = 1$ , $\alpha = 0$ and $\theta = \pi / 2$ as follows:

$$I\left(x, y, z_i\right) = I_0 \left[ 1 + t^2 + \tau^2 + 2t\tau \cos\left(\phi - \frac{\pi}{2}\right) - 2t \cos\phi \right] \tag{3.7}$$

where the transmission of the object $t^2$ and the phase dot $\tau^2$ are 0.85. The fitting parameter $I_0$ is found to be $I_0 = 35$ pixel readouts (with an error of ~11%). The incoming intensity $I_0$ in nW per pixel is then

$$35 \times 0.0025 \sim 0.088 \frac{nW}{\text{pixel}}. \tag{3.8}$$

As before, we compare this value with the intensity per pixel calculated from a known imaging beam with total power of $P = 76\,\mu\text{W}$:

$$I_{0\ \text{per pixel}} = \frac{2P}{W_0^2 \pi} \times \text{pixel area} = \frac{2 \cdot 76\ \mu\text{W}}{\left(4 \times 10^{-3}\right)^2 \pi} \times 36 \times 10^{-12} = 0.1\ \text{nW/Pixel}. \tag{3.9}$$

Here we found the intensity per pixel calculated by the measured ingoing power to be 12% higher but close to the error range. For this measurement not only was the imaging beam attenuated by the optics as discussed above, but also some low spatial frequency components propagated through the phase dot, reducing the signal. (As mentioned before, the signal upon phase contrast imaging stems from interference of the scattered components with the unscattered ones).

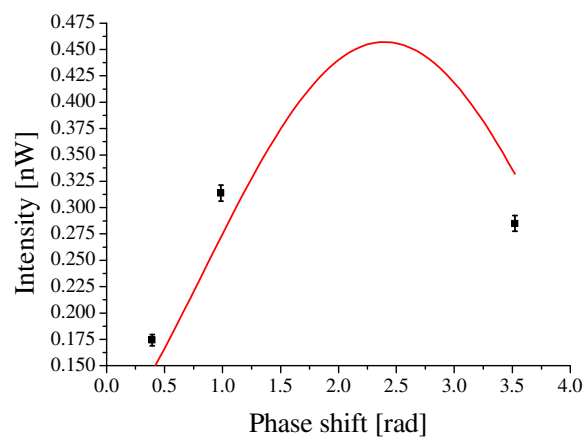


Figure 3.5 - Signal of phase contrast images $< S >$ for the same settings as in Fig. 3.4 except for a single data point at $\pi/2$ rad as this specific dot (200 µm diameter, 137 nm thickness) was used as the Fourier filter in this setup. Red curve denotes the fit according to theoretical phase contrast signal as discussed above.

## 3.5 Resolution

Let us consider the resolution limits of our imaging system theoretically and experimentally. In this section we show results of resolution measurements with dielectrics.

In general, optical *resolution* is defined as the distance $\mathfrak{R}$ between two separated points which can be resolved. We adopt here the resolution criterion defined by Rayleigh as the distance between two peaks of Airy functions when the peak of the first Airy pattern is located on the first minimum of the second Airy pattern as in Fig. 3.6. Any focal imaging system is diffraction-limited as we cannot make ideal aberration-free infinitely large lenses.

With our diffraction-limited imaging lens one would expect the resolution limit $\mathfrak{R}_{\text{optical}}$ to be [Hec02]:

$$\mathfrak{R}_{optical} = 1.22\frac{\mathrm{f}_1\lambda}{\mathfrak{D}} \tag{3.10}$$

where $f_1$ is the focal length and $\mathfrak{D}$ is the diameter of the lens. In our case we have used $\mathrm{f}_1$=100 mm and $\mathfrak{D}$=30 mm, such that R~2.5 μm. For other experiments we used lenses with different focal length ($\mathrm{f}_1 = 200\,\mathrm{mm}$ and $\mathrm{f}_1 = 300\,\mathrm{mm}$) and the resolution increased accordingly. For our diode laser at $\lambda = 780\,\mathrm{nm}$ the resolution grew to 3 μm for $\mathrm{f}_1 = 100$ mm or 9 μm for $\mathrm{f}_1 = 300$ mm.

One can resolve between two points if their generated signal is separated by at least two pixel sizes. This introduces the pixel resolution limit and together with the lens diffraction limit defines the minimal spacing we can resolve. Although we use a camera with a pixel size of 6 μm, the effective pixel resolution $\mathfrak{R}_{\text{pixel}}$ may be better because it is magnification-dependent, as follows:

$$\mathcal{R}_{pixel} = \frac{2 \times (\text{pixel size})}{M}, \tag{3.11}$$

where $M$ is the magnification. For the magnification $M = 2$ that we used our pixel resolution limit is $\mathcal{R}_{pixel} = 6$ µm. In our example the resolution is limited by the pixel size. In particular in the case of demagnifying by 2 we get $\mathcal{R}_{pixel} = 24\,\mu\text{m}$.

Let us estimate our actual imaging resolution by looking at the edge of a dark-ground image of a 200 µm square with thickness of 314 nm magnified by two. We used a 200 µm opaque disk Fourier filter and reduced probe power to 41 µW. We compared the edge variation from the dark-ground image, Fig. 3.7, to the edge slope measured using a high resolution low force stylus profiler (Veeco Dektak 8) as presented in Fig. 3.8. The edge measured with the high resolution force stylus profiler was 4 µm; but using the dark-ground technique, we found a slope width of 4 pixels equivalent to 24 µm; considering a magnification of 2 we found the limit two times higher than our pixel resolution. This comparison suggests that our imaging resolution is limited not merely by the pixel size merely but by optical aberrations as well.

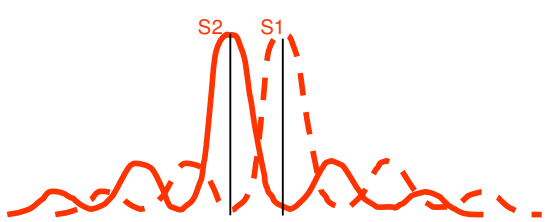


Figure 3.6 – Rayleigh criterion definition for the resolution limit. Two Airy functions originating from light due to two distant point sources, which is focused by a lens of diameter $\mathcal{D}$ overlap such that the peak of S1 is at the minimum of S2 and vice versa.

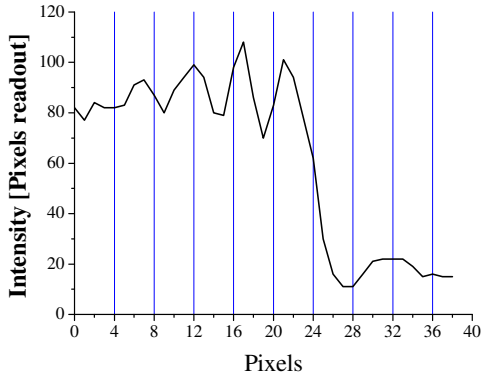


Figure 3.7 – One-dimensional plot of the squared intensity versus location. This plot was done at several cross-sections of the square and found to be consistent. A diffraction pattern can be seen as the signal fluctuates periodically. This artifact cannot be usually seen in atomic clouds, as the phase shift near the edges is slowly varying.

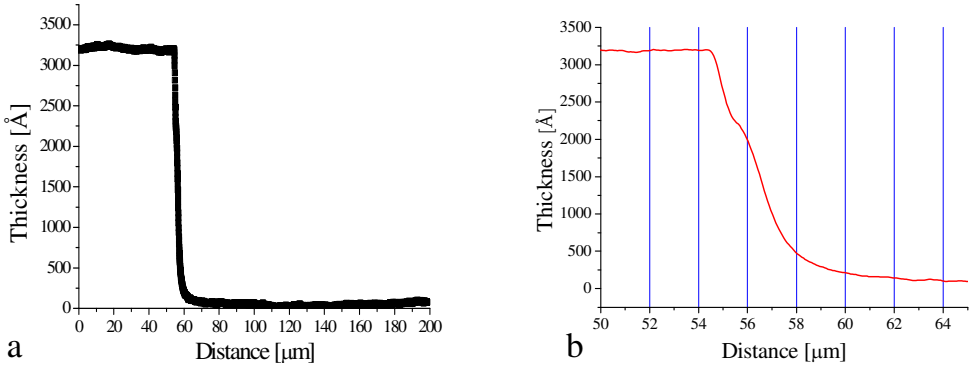


Figure 3.8 (a) The slope of the fabricated ITO square is about 4 μm as measured by a low force stylus profiler, the mean thickness is 314 nm, (b) The slope in a zoomed in plot.

# Chapter 4

# Imaging techniques applied to cold atoms

In this chapter we investigate the different imaging methods applied to our laser-cooled atomic clouds released from a magneto-optical trap (MOT) [Met03]. The imaging experimental setup is described in section 4.1. An associated algorithm to extract information from the data is described in section 4.2. Following our review of theoretical ideal expected signals, we show our results and conclude with a short discussion of the SNR for different imaging methods. Finally, we extract the atomic density from absorption and dark-ground imaging.

## 4.1 Imaging apparatus

We image a ~400 μK atomic cloud with roughly $10^7 - 10^8$ atoms. The cloud's Gaussian shape has a width of roughly 1.8 mm at 1/e of the maximum. Imaging our atoms requires considerable care with alignment. The diode laser (Toptica DLX110), tuned to the $^{87}$Rb hyperfine $F = 2 \rightarrow F' = 3$ transition at 780 nm, is difficult to align as its light is not visible (in the near infrared) and a special viewer is required. The imaging probe beam passes through a polarization-maintaining optical fiber before expansion into a 20 mm diameter beam by a collimator (Schäfter-Kirchhoff output lens f=100 mm) as depicted in Fig. 4.1. During our imaging experiments we often need to maintain constant laser intensity so we split the beam from the fiber equally, with one portion of the light going into a photo diode (ThorLabs PDA55) for measuring the intensity of each imaging pulse.

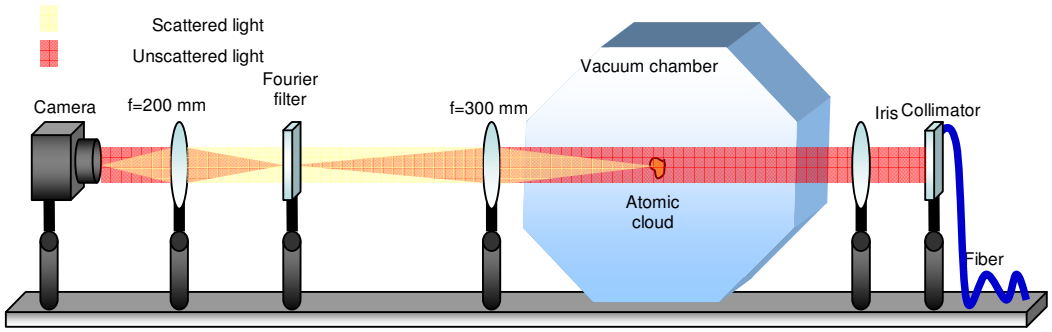


Figure 4.1 – Optical layout of the cold atoms imaging experiment.

The expanded beam crosses the vacuum chamber and passes through the cloud before propagating to the object lens (f=300 mm). At the focal plane a micrometer-driven translation stage is placed to align the Fourier filter. The filter's size should completely encompass the (calculated) probe spot size of 7.5 μm at the focal point. The size of the filter is also based upon the expected size of the Fourier image of the object, which was intended to be a BEC of a size on the order of 100 μm. According to Eq. (3.1) such a cloud would have a Fourier image with a diameter of 1.2 mm (at 1/e), which is much larger than the size of the Fourier filters actually used. The transmitted light propagates through a second lens (f=200 mm) to form an image at its focal point, exactly where the camera is placed.

Demagnification is essential to image relatively large clouds with our camera, whose chip size is 2.8 mm×4.5 mm. All the optical components after the vacuum chamber (on the left-hand side of the chamber) are placed on an optical rail for easy optimization of their positions, and of the Fourier filter in particular.

The experiment is conducted in cycles; at the end of each cycle the atoms are released and a 100 μs-long imaging pulse is applied after 5 ms of free fall under gravity. Five seconds later another such pulse is applied to image the probe beam when no atoms are present. All data acquisition is done by a Labview interface under our experimental control.

The imaging beam is calibrated initially using an absorption imaging configuration, with an acousto-optic modulator (AOM from IntraAction, model ATM1001A2) used to detune the probe light from resonance. The AOM may be adjusted for negative (i.e. red) and positive (i.e. blue) detuning. For each experiment we use a different Fourier filter: for dark-ground imaging we place a 100 μm-diameter chromium disc at the Fourier plane and for phase contrast imaging we use a 200 μm ITO square of 137 nm thickness to impose a ~$\pi$/2.5 phase shift on the unscattered light.

## 4.2 Image analysis

The cloud's atomic density distribution is not detected straightforwardly on the camera, and we therefore apply an algorithm to extract it from the images taken. We wish to calculate the number of atoms imaged per pixel using the three imaging methods (absorption, dark-ground and phase contrast).

Let $I_0$ be an image of the probe beam taken without atoms at the end of each cycle when all other light sources in the chamber are off. Let $I_{abs}$, $I_{pc}$ and $I_{DG}$ be the images taken without any Fourier filter (absorption), with an ITO square as a Fourier filter (phase contrast), and with an opaque disc as a filter for dark-ground imaging respectively. We use $I_{\text{Im-beam}}$ as the image of the incoming probe beam before the atomic cloud. Ideally, the incoming beam $I_{\text{Im-beam}}$ is the same as $I_0$ for absorption and phase contrast configurations, but not for dark-ground imaging. Therefore, it is essential to distinguish $I_{\text{Im-beam}}$ from $I_0$ in any dark-ground analysis.

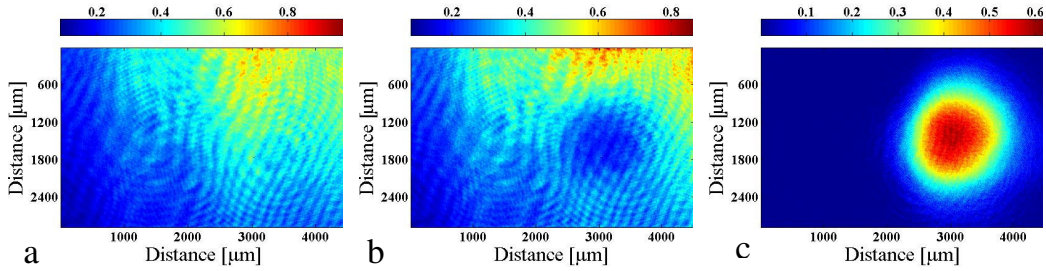


Figure 4.2 Images taken during a cycle with a probe power of 130 μW, +7 MHz blue-detuned from resonance. (a) Imaging beam without the atoms, denoted by $I_0$. (b) Absorption image, i.e. $I_{abs}$. (c) The atomic cloud's shape $S_{abs}$ from Eq. (4.1). The colors correspond to normalized intensities.

For absorption imaging we find the cloud shape simply by subtracting the shadow image $I_{abs}$ from the imaging beam $I_0$ and dividing it by $I_0$, yielding the normalized signal:

$$S_{abs} = \frac{I_0 - I_{abs}}{I_0}. \tag{4.1}$$

Most of the noise inherent in the imaging beam is cancelled by this normalization (Fig. 4.2).

Retrieving the cloud's shape from a dark-ground image is straightforward as this method produces scattered light (the signal) on a dark background. In Fig. 4.3, we subtract the background ($I_0$) from the dark-ground image ($I_{DG}$) to find the cloud's shape:

$$S_{DG} = \frac{I_{DG} - I_0}{I_{\text{Im-beam}}}. \tag{4.2}$$

As before, we normalize the signal with respect to the imaging beam intensity $I_{\text{Im-beam}}$ (Fig. 4.2(a)) in order to derive an absolute ratio correlated to the optical density. The imaging beam is measured without the opaque dot.

We emphasize that in the dark-ground configuration, the unscattered beam is blocked and $I_0$ should be zero. But if unscattered light still reaches the detector (if,

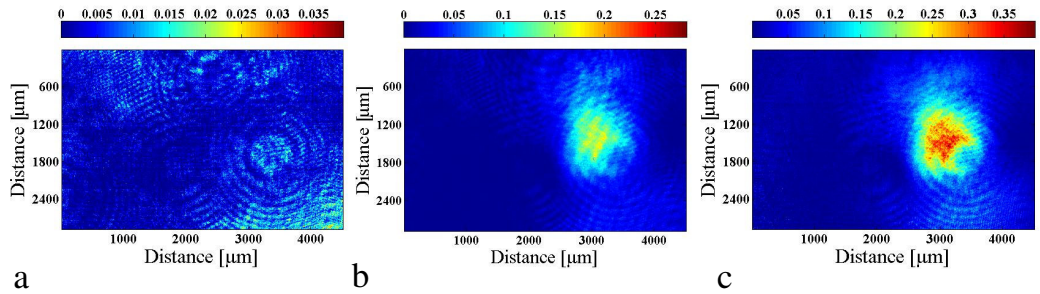


Figure 4.3 – Images taken with a dark-ground configuration during a cycle with a probe power of 130 μW, +7 MHz blue-detuned from resonance. (a) Imaging beam without the atoms $I_0$, blocked by an opaque dot at the Fourier plane. (b) Dark-ground image $I_{DG}$. (c) The atomic cloud's shape $S_{DG}$ from Eq. (4.2). The colors correspond to normalized intensities.

for example, the dot is improperly aligned or too small) or noise of any kind causes a non-vanishing reading, the background subtraction will eliminate this false signal. But we cannot completely eliminate the noise inherent in the imaging beam (as we did for absorption) because another imaging pulse is needed (to obtain $I_{\text{Im-beam}}$) for each cycle without the opaque dot, and this requires changing the alignment for each cycle.

In this experimental configuration, we need to ensure that the images correspond to dark-ground imaging and not simple fluorescence. This requires us to distinguish forward scattered photons from spontaneously scattered photons; although we imaged off resonance, spontaneous scattering may be significant.

In order to rule out spontaneous emission as a source for the image signal, we changed the imaging apparatus as depicted in Fig. 4.4(a). This imaging configuration should produce only a fluorescence signal, since the camera is not aligned with the imaging beam, i.e. since we are imaging the cloud from the side. We placed an additional mirror (M3 in Fig. 4.4(a)) in order to reflect the light from the opposite direction of the cloud. This was done to exclude the possibility of defocusing due to the momentum kick the atoms had suffered from a resonant

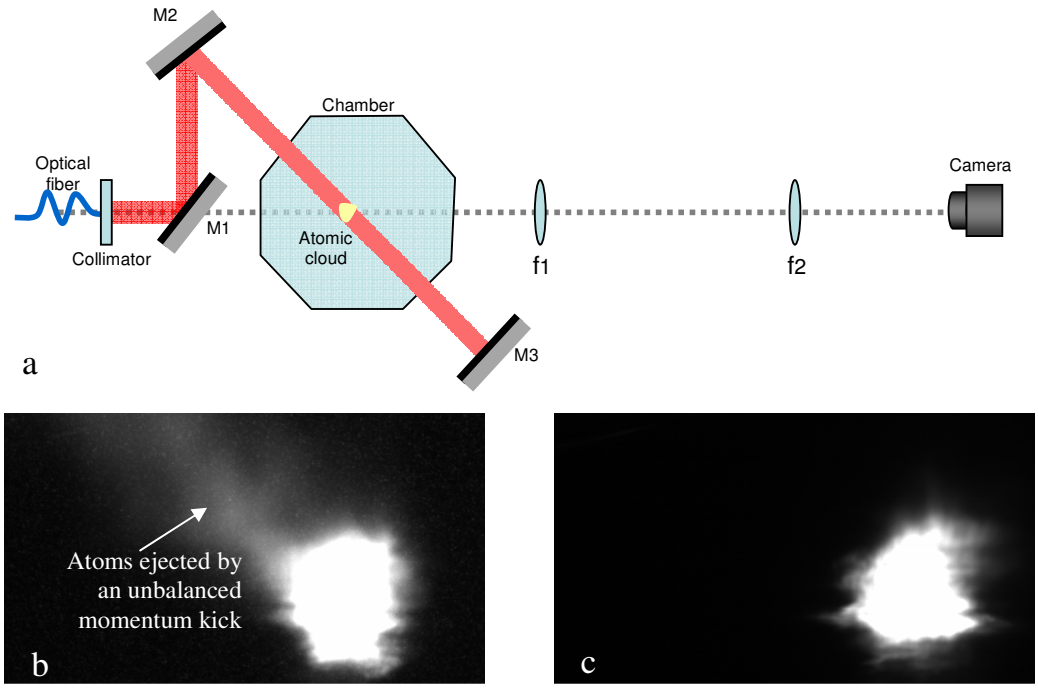


Figure 4.4 – Fluorescence imaging of atoms in a MOT. (a) Imaging setup, the probe laser beam deviates from the detector's optical axis ($f_1$=300 mm, $f_2$=200 mm) then reflected by M3 through the chamber to impart a balanced momentum kick from the opposite direction. (b) An image taken without the balancing reflecting mirror (M3). The atoms suffer a momentum kick upon absorbing the off-axis probe beam, ejecting some from the cloud. (c) A balancing reflecting mirror (M3) placed so that two counter propagating probe beams maintain the cloud's shape in center.

imaging beam. To confirm the mirror alignment, we used the fluorescence imaging configuration and imaged before releasing the trap (Fig. 4.4(b) and 4.4(c)). When we applied an imaging pulse after 5ms of free fall under gravity, we found no signal on resonance and we thus conclude that spontaneously scattered photons do not create a sufficiently large signal to be detected.

We can now be sure that the signal we observe in the dark-ground configuration results from forward scattered photons and not from spontaneous emission.

The last imaging method requires more effort to extract the data. Due to time constraints, we use a 200 μm-square phase dot which was large enough to align easily. Such a relatively large filter transmits unscattered light as well as a large quantity of scattered light. Hence, the output signal is similar to absorption. In the following we describe the image analysis used to recover the contribution of phase-

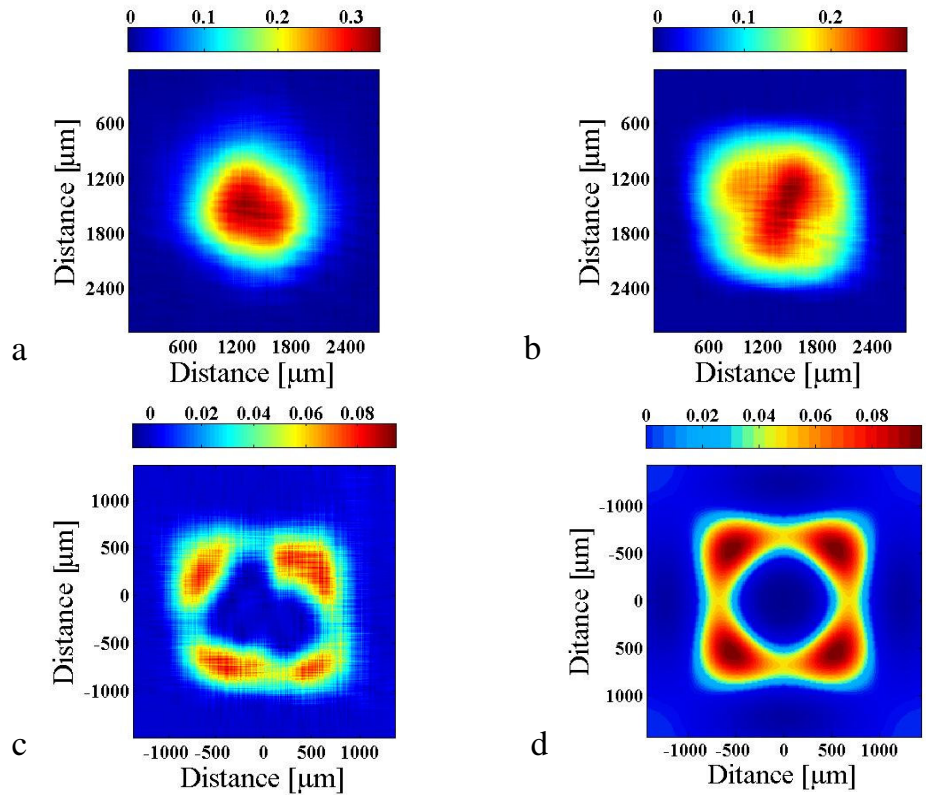


Figure 4.5 – Images analyzed to provide normalized phase-contrast image. Images are obtained from two different cycles, first without a phase shifter and then with. The probe intensity is 130 μW, -5 MHz red-detuned from resonance, and the Fourier filter is a 200 μm square. (a) Atomic cloud retrieved from an absorption image $S_{abs}$. (b) Atomic cloud retrieved from data taken in a phase contrast configuration i.e. $(I_0 - I_{pc})/I_0$. (c) Subtraction of 'a' from 'b' i.e. $S_{pc}$. (d) Simulated signal using the same experimental parameters; all negative values are replaced by zero.

contrast interference from an image comprising absorption mixed with phase contrast.

For each cycle using a phase contrast configuration we measure another cycle using an absorption configuration with the same parameters, i.e. we run cycles with the phase dot and cycles without it. Then we subtract the images and define the signal as

$$S_{pc} = \frac{\left(I_0 - I_{pc}\right)}{I_0} - \frac{\left(I_0 - I_{abs}\right)}{I_0}, \tag{4.3}$$

where $I_0$ is the imaging beam pulse with the phase dot for $I_{pc}$, and without the phase dot for $I_{abs}$) (Fig. 4.5). One cannot simply define $S_{pc} = \left(I_{abs} - I_{pc}\right)/I_0$ because $I_0$ may be different for each cycle.

The phase contrast analysis reveals different parts of the cloud for different detuning. Basically, a small part of the high spatial frequencies scattered light passes outside the phase dot creating the phase contrast signal. Subtracting $I_{pc}$ from the absorption signal $I_{abs}$ leaves the periphery because the optical density at the edge of the cloud changes radically, creating high spatial frequency in the Fourier plane. These high spatial frequencies component pass outside the large phase dot and therefore interfere with the unscattered light. The reason for large angle scattering for these spatial components stems from the Heisenberg uncertainty principle as the momentum increases when light is confined to pass through an aperture. For opposite detuning we extract a “negative” image of the former as shown in Fig. 4.6 and Fig. 4.7. This intensity flipping caused by the sign change of the phase shift, separates fast from slowly varying spatial frequencies on the image plane.

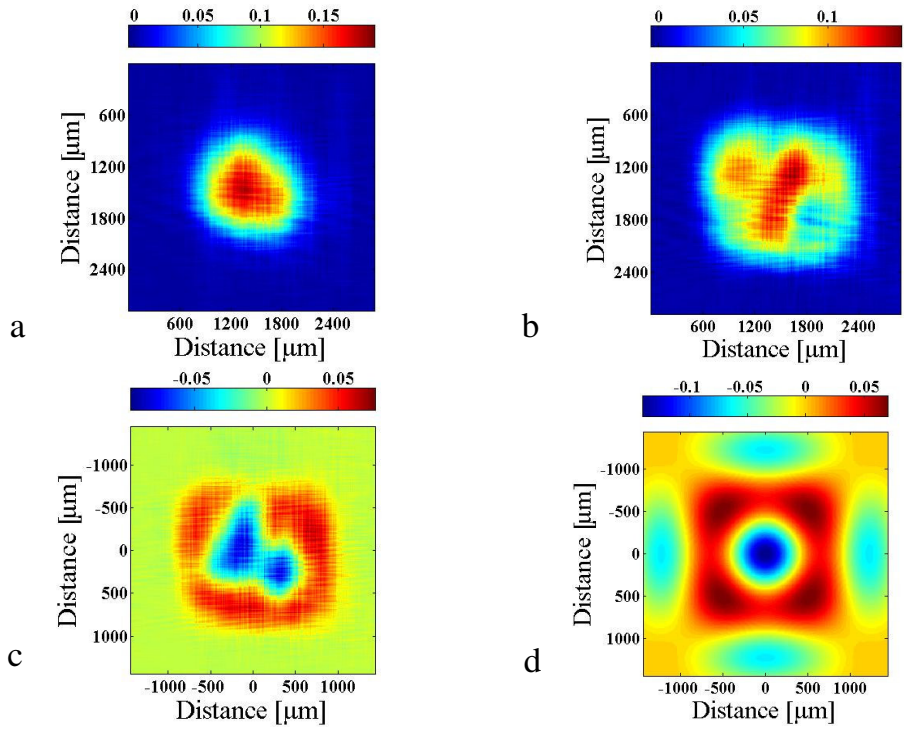


Figure 4.6 – Phase contrast imaging. (a)-(d) same as Fig. 4.5 but with -12 MHz red detuning.

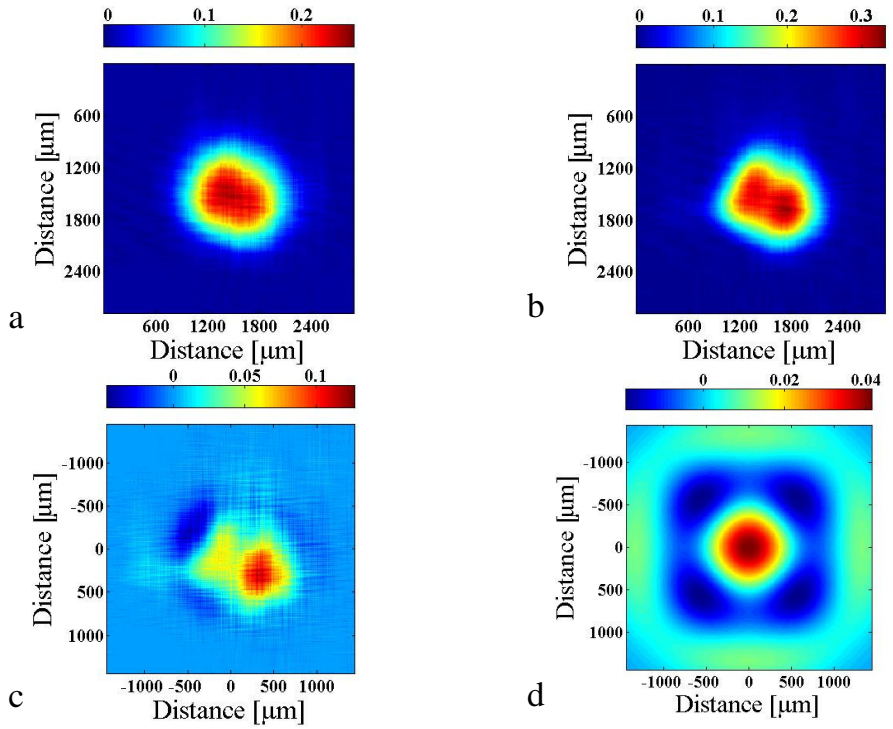


Figure 4.7 - Same as Fig. 4.6 but with +12 MHz blue detuning.

## 4.3 Theoretical ideal signals

In order to lay the theoretical basis for interpreting the experimental results, we first examine the expected imaging signal for the ideal case in which noise-free probe light is used with Fourier filters that sharply distinguish between unscattered light and light scattered from the imaged atoms. We consider $^{87}$Rb, for which the $^{2}P_{3/2}$ excited level has a natural linewidth of $\gamma = 6$ MHz.

For absorption imaging we use Eq. (4.1) and Eq. (2.53) to derive the output signal; the cloud shape is given ideally by

$$\mathrm{S_{abs}} = \frac{I_0 - I_{abs}}{I_0} = 1 - t^2 = 1 - e^{-OD\frac{1}{1+\Delta^2}}, \tag{4.4}$$

where $t$ is the transmission, such that $I_{abs} = I_0 t^2$ is the absorption signal as defined in Eq. (2.67), $OD$ is the optical density and $\Delta$ is the detuning in units of $\gamma/2$. The signal is reduced either by increasing the probe's detuning from resonance or by reducing the optical density (Fig. 4.8).

Figure 4.9 shows the behavior of the ideal dark-ground signal (Eq. (4.2) with $I_0 = 0$), which is given by Eq. (2.68):

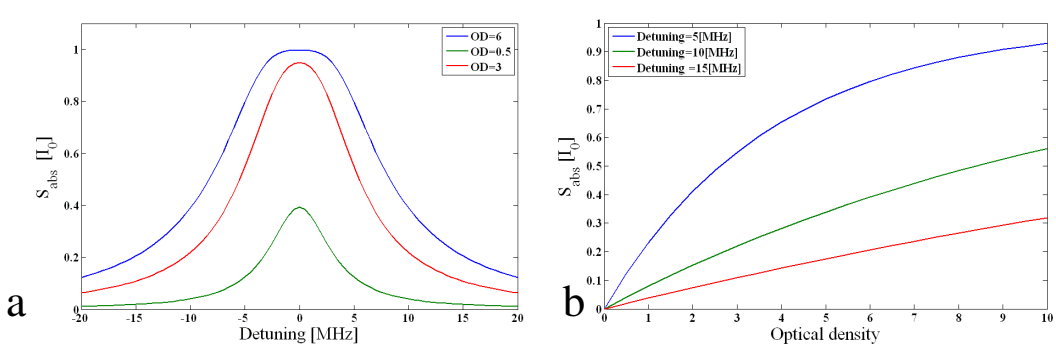


Figure 4.8 – (a) Theoretical normalized absorption signal $S_{abs}$ versus detuning for different optical densities. (b) $S_{abs}$ versus optical density for fixed detuning.

$$S_{DG} = \frac{I_{\text{theoretical_DG}}}{I_{\text{Im-beam}}} = t^2 + 1 - 2t\cos(\phi). \tag{4.5}$$

Substituting $t$ and $\phi$ according to Eq. (2.52) and Eq. (2.54), we find the optical density dependence:

$$S_{DG} = 1 + e^{-OD\frac{1}{1+\Delta^2}} - 2\left(e^{-\frac{OD}{2}\frac{1}{1+\Delta^2}}\right)\cos\left(-\frac{OD}{2}\frac{\Delta}{1+\Delta^2}\right). \tag{4.6}$$

In Fig. 4.9(a) we see that the dark-ground signal has a dip at resonance if the optical density is larger than 3.5. On the other hand, we see from Fig. 4.9(b) that the maximum signal is achieved for detuning of $\Delta = 1$ at an optical density of about $OD = 8$.

Let us assess the dark-ground signal in a non-ideal measurement. First we quantify the effect of the opaque dot on the atomic cloud diffraction pattern as follows: for a Gaussian-shaped atomic cloud of 1.8 mm width at 1/e one finds a Gaussian intensity distribution of diameter d ≈ 85 μm at 1/e in the Fourier plane. A 100 μm diameter opaque dot placed in the Fourier plane then allows only a small fraction of the scattered light to pass, as given by the ratio between the intensity integrated over $r > 50\,\mu\text{m}$ (outside the dot) and the incident intensity:

$$I_{total} = \frac{\int_{50}^{\infty} e^{-\frac{r^2}{(d/2)^2}} r dr}{\int_{0}^{\infty} e^{-\frac{r^2}{(d/2)^2}} r dr} = e^{-\left(\frac{100}{85}\right)^2} = 0.25, \tag{4.7}$$

suggesting that we have to multiply the detected dark-ground signal by a factor of 4 in order to recover the intensity predicted by the ideal dark-ground imaging. Evidently, this factor is slightly higher than the one we find experimentally, as discussed in the next section.

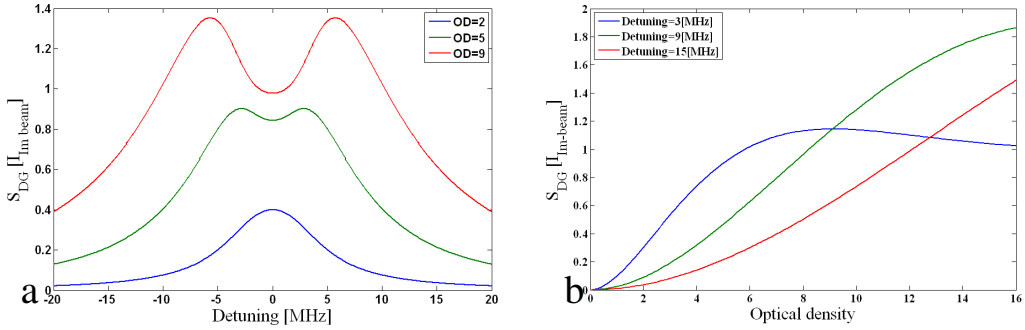


Figure 4.9 – (a) Dark-ground signal versus detuning for several optical densities. (b) Dark-ground signal versus optical density for different detuning. The maximum intensity (~1.25 $I_{\mathrm{Im}-beam}$ ) for dark-ground imaging at detuning of half atomic linewidth i.e. $\Delta = 1$ (blue curve) is obtained at *OD* of ~8.

Finally, we refer to the phase contrast analysis algorithm in section 4.2. The theoretical signal for ideal phase contrast imaging is given by

$$S_{pc} = I_{abs} - I_{\mathrm{theoretical_}pc} = -I_0 \left\{ 2 - 2\sqrt{2}t \cos\left( \phi + \frac{\pi}{4} \right) \right\}. \tag{4.8}$$

Ideally the signal is negative at negative detuning (due to the positive phase shift) and positive at positive detuning (due to a negative phase shift), but it is not anti-symmetric around resonance as depicted in Fig. 4.10. This is due to the fact that the near-resonant phase contrast signal involves contributions from absorption and from the phase shift. While the contribution due to the phase shift is anti-symmetric and the contribution of the absorption is symmetric, the total signal turns out to be non-symmetric.

In our case the phase shift imparted by the phase dot is $\pi/2.5$. This phase dot was made to impart a $\pi/2$ phase shift for initial tests with a HeNe laser beam, but it was later used with the diode laser at 780 nm. The use of a non-ideal phase dot reduces the signal intensity as depicted in Fig. 4.11. Moreover, the phase dot is large compared to the Fourier image (at 1/e) of the atomic cloud. This implies that the absorption component of the phase contrast image dominates the contribution of the phase shift. An analysis of our experimental results follows.

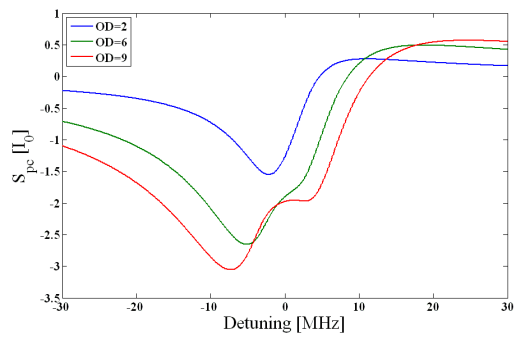


Figure 4.10 – Phase contrast imaging, showing the theoretical normalized signal $S_{pc}$ for various optical densities and an ideal phase dot that imparts a phase shift of $\pi/2$ to the unscattered light.

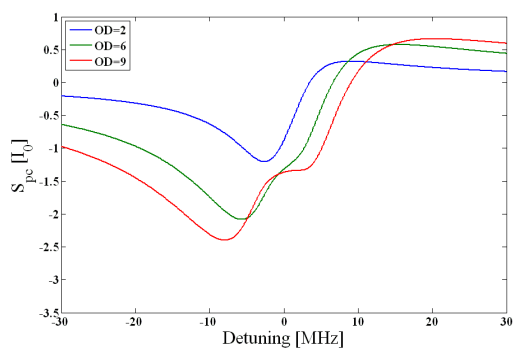


Figure 4.11 – The same plot as in Fig. 4.10 but with a non-ideal phase dot which imparts a phase shift of $\pi/2.5$ to the unscattered light.

## 4.4 Signal and noise analysis

In this section we present signal and noise analysis of the measurements. We analyze the signal at the center of the cloud image as a function of detuning frequency for the different imaging methods.

Several images were taken (three for absorption and five for dark-ground) for the same detuning and the average signal $\langle S \rangle$ was calculated over a 10x10 pixel matrix at the centre of the cloud's image. Let us define the noise as the standard deviation $\sigma_s$ of the selected 100 pixels. This definition of the noise is associated with the signal, i.e., the atomic density, and with noise inherent in the laser beam. Using a 10×10 area out of the entire image of roughly 200×200 pixels ensures that the atomic

density variation and the imaging laser beam intensity distribution (although it is normalized) can be neglected. The same analysis was done for an area close to the edge of the frame with a mean value for the background of $\langle B \rangle$ and associated standard deviation $\sigma_B$. For noise inherent in the signal (such as shot noise and noise added from the optics) we define the SNR as

$$SNR = \frac{\langle S \rangle}{\sqrt{\sigma_S^2}} \cdot \tag{4.9}$$

Let us define the signal to background noise ratio i.e. noise inherent in the camera as readout noise or dark current noise or noise arising from the background intensity:

$$SNR = \frac{\langle S \rangle}{\sqrt{\sigma_B^2}} \cdot \tag{4.10}$$

For all imaging methods we maintain the same incoming probe imaging beam power of 130 μW. This intensity was chosen to keep the camera below saturation on the one hand, and on the other hand, to get sufficiently high signal intensity. For absorption and phase contrast imaging the probe beam enters the camera with little intensity reduction and this sets an upper limit. For dark-ground the incoming probe beam is filtered and we wish to detect significant signal thus setting a lower limit. Furthermore, for all plots, the error bars are the standard deviation of a few images taken at the same settings.

For dark-ground imaging, we plot the signal and the SNR as a function of detuning (Fig. 4.12). We use Eq. (4.6) to fit the data and find the optical density to be 7.8. In this plot we observed a clear dip at resonance as suggested by Fig. 4.9(a).

For phase contrast, as discussed above, we could not perform a quantitative analysis for the number of atoms nor for the SNR because the Fourier filter was too

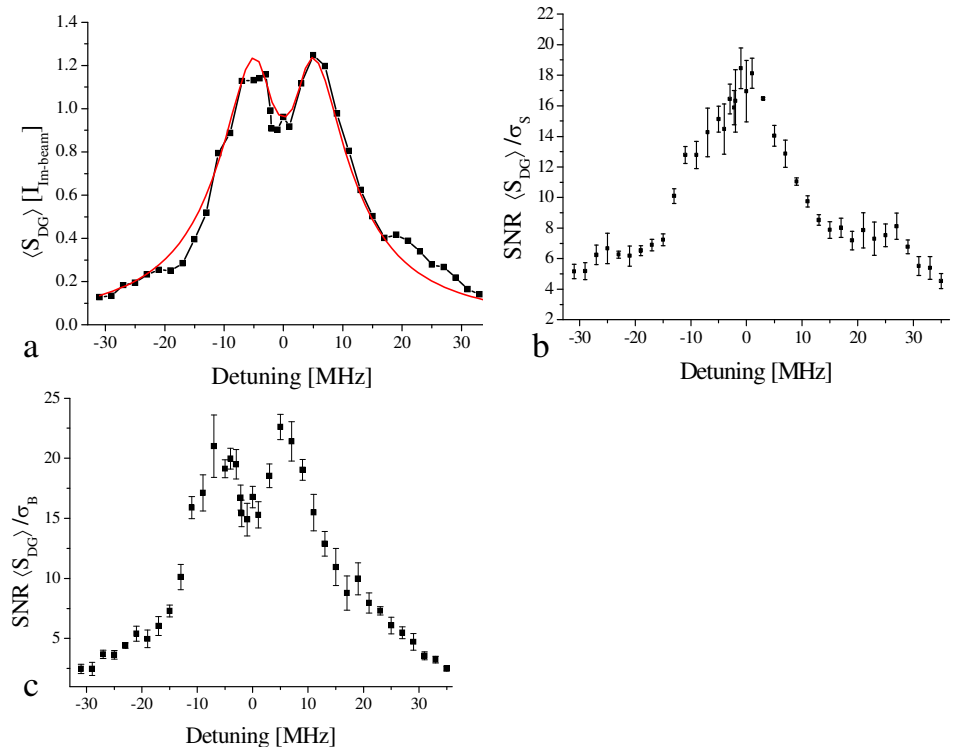


Figure 4.12 – (a) Normalized dark-ground signal $< S_{DG} >$ versus detuning. From the fit, the free parameter which is the peak optical density was found to be 7.8 (b) Signal to noise ratio i.e. $< S_{DG} > / \sigma_S$. (c) Signal to background noise ratio i.e. $< S_{DG} > / \sigma_B$, the dip is clearly observed as the background noise is nearly constant. All error-bars are the standard deviation of 5 pictures taken at the same detuning.

large and therefore affected most of the scattered light also, giving rise to images similar to standard absorption.

In Fig. 4.12(a) we normalize the on-resonance signal rather than its maximum; the latter is seen to be ~1.25 times the incoming intensity. This is the maximum theoretical signal that occurs at a detuning of 3 MHz, as shown in Fig. 4.9(b). As discussed in section 4.3, multiplication of the dark-ground signal by a factor is necessary because the opaque dot blocks some of the scattered light and decreases the signal. The best fit to our results is for the signal multiplied by 3 (compared to the theoretical value of 4). This suggests that either the cloud is smaller than 1.8 mm at 1/e or the probe light intensity ($I_{\text{Im-beam}}$) is somewhat higher than an average imaging pulse. Although the signal was multiplied by a factor of 3, the noise usually

contains high Fourier components, which would anyway be transmitted outside the opaque dot. Hence, optimizing the Fourier filter's size would improve the SNR.

For absorption imaging, we find the highest signal on resonance and a peak optical density of ~5 (Fig. 4.13(a)). We found that the signal-to-background noise ratio (shown in Fig. 4.13(c)) varies. This variation stems from the noise inherent in the camera and from intensity fluctuations of the imaging beam between the two pulses used for each cycle. One can neglect the camera noise because it is small and constant with detuning (as one can see from the dark-ground analysis). But the intensity fluctuations between pulses of the imaging beam are definitely affecting the SNR of absorption, bearing in mind that such fluctuations do not occur for dark-ground imaging because the imaging beam is blocked. In Fig. 4.13(b) the SNR is low off-resonance because the absorption is weak; conversely, the on-resonance SNR is very high because almost all the light is absorbed.

Comparing signal-to-noise ratios for absorption and dark-ground imaging allows us to identify the feature that makes phase detection imaging methods preferable to absorption imaging when using far-detuned light in non-destructive imaging.

In Fig. 4.14 we compare the SNR graphs plotted above for absorption and dark-ground imaging. When examining the curves far enough from resonance the SNR for dark-ground imaging exceeds that for absorption. If large detuning is used, the absorption signal drops, but the phase shift drops more slowly (Fig. 2.10) and phase detecting imaging methods exhibit superior SNR. Therefore one can use large detuning and keep the absorption negligible while maintaining roughly the same amount of atoms in the cloud after each imaging pulse (non-destructive imaging).

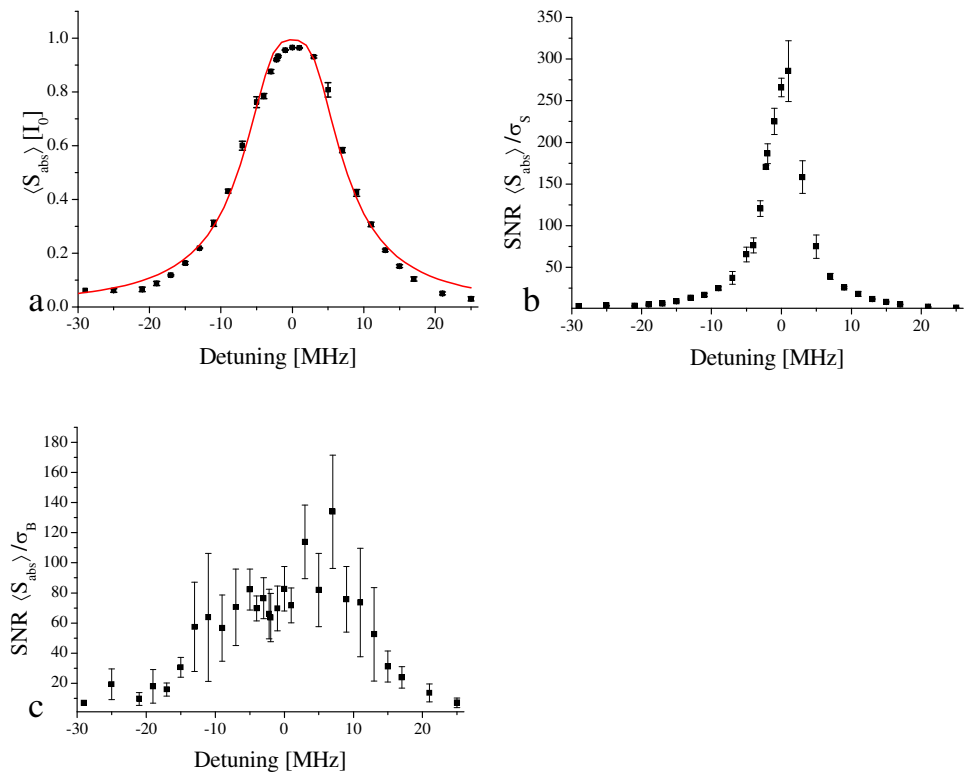


Figure 4.13 – Absorption imaging. (a) Average signal $<S_{abs}>=<1-t^2>$ of three images as a function of detuning; the fit corresponds to an optical density of 5.2. (b) Signal-to-noise ratio i.e. $<S_{abs}>/\sigma_S$ (c) Signal-to-background noise ratio i.e. $<S_{abs}>/\sigma_B$; error bars are the standard deviation of 3 cycles with the same settings.

## 4.5 Derivation of atomic density

We now analyze the dark-ground image shown in Fig. 4.3 to find the number of atoms in the cloud. Ideally, when a far detuned (non-destructive) probe beam is used, one would directly calculate the phase shift per pixel from the intensity [Ket99], as the transmission for large detuning can be regarded as $t \sim 1$. The phase shift is then extracted using Eq. (2.68):

$$I\left(x, y, z_i\right) \sim I_{\text{Im-beam}} \left\{2 - 2\cos\left(\phi\right)\right\}, \tag{4.11}$$

where here $I_0$ denotes the intensity of an incoming imaging beam. However, in our experiment the absorption was not negligible, hence, we used a general expression

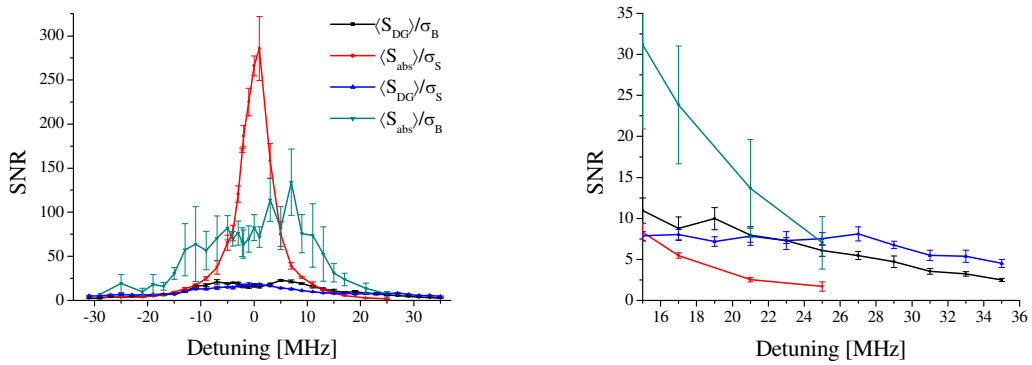


Figure 4.14 – (a) Comparison for all SNR plots: for absorption imaging the red and the green are the signal to cloud's center and background noise ratio respectively. For dark-ground, the blue and black curves are the ratio of the signal to cloud's center and background noise respectively. (b) The dark-ground SNR exceeds absorption's far from resonance.

as shown in Eq. (4.5). The intensity detected is optical-density-dependent according to Eq. (4.6) (Fig. 4.15(a)). A separate image of the unblocked imaging beam ($I_{\text{Im-beam}}$) was taken and used to find the normalized signal intensity. Ideally, one would extract the optical density in each pixel from $S_{DG}$ but, as explained in section 4.3, the dark-ground signal $S_{DG}$ is multiplied by 3. Applying Eq. (4.6) (with the additional factor of 3) to each pixel results in optical density per imaged area in a single pixel ($OD_A$), and the number of atoms in an imaged area per pixel is then (Appendix C) (Fig. 4.15(b)):

$$N_A = \frac{OD_A \cdot A}{\sigma_0}, \tag{4.12}$$

where $A = \text{pixel area}/\text{magnification}$. The total atom number is then

$$N_{\text{total}} = \sum_{\text{pixels}} \frac{OD_A \cdot A}{\sigma_0} \sim 9.4 \times 10^7 \text{ atoms}. \tag{4.13}$$

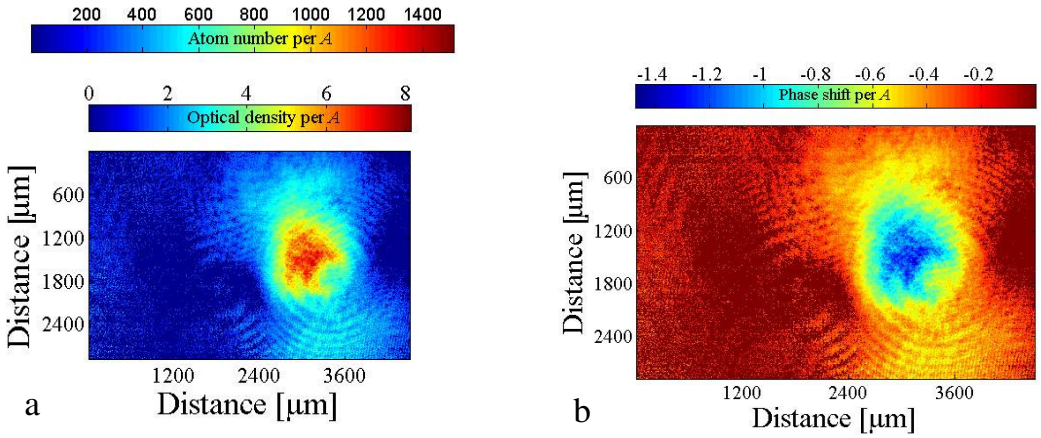


Figure 4.15 – Dark-ground images (a) The color-bar exhibits optical density and number of atoms. (b) The color-bar is the phase shift retrieved in each pixel, the phase shift is negative as the detuning was +7 MHz to the blue.

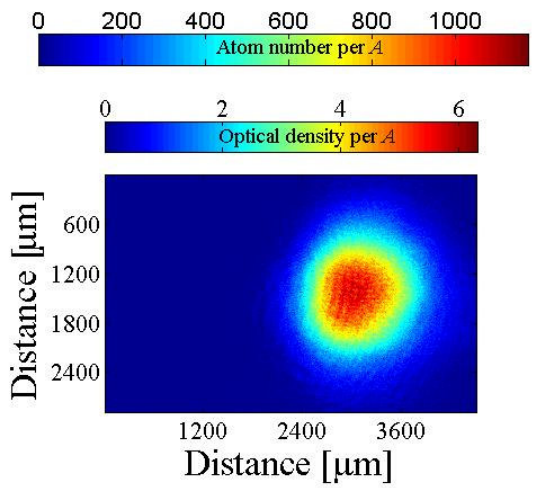


Figure 4.16 – Absorption images with different color scales (a) The color-bar exhibits optical density and the number of atoms.

Let us find the number of atoms extracted from absorption imaging (Fig. 4.2). Ideally (regardless of any noise), one would find the transmission per pixel on resonance by dividing the atom's image by the probe's image i.e. [Ket99],

$$I_{abs} = I_0 t^2 = I_0 e^{-OD},$$
$$N_{total} = \frac{A}{\sigma_0} \sum_{pixels} -\ln(t^2). \tag{4.14}$$

But in our case we measured the transmission at blue detuning of +7 MHz. Thus, the optical density for each pixel was calculated by (Fig. 4.16(a)):

$$S_{abs} = \frac{I_0 - I_{abs}}{I_{\text{Im-beam}}} = 1 - e^{-OD\frac{1}{1+\Delta^2}} . \tag{4.15}$$

Or we can find the optical density:

$$OD = \left(1+\Delta^2\right)\ln\left(\frac{I_0}{I_{abs}}\right). \tag{4.16}$$

Applying Eq. (4.16) to each pixel results in an optical density per imaged area $A$ in a single pixel ($OD_A$), and the number of atoms in an imaged area per pixel is again (Fig. 4.16(b)):

$$N_A = \frac{OD_A A}{\sigma_0} . \tag{4.17}$$

The sum of all pixels result in the total atom number is then

$$N_{\text{total}} = \sum_{\text{pixels}} \frac{OD_A A}{\sigma_0} \sim 4.9\times10^7 \text{ atoms} . \tag{4.18}$$

Here, we found a peak optical density of 6, however, in the previous section (4.4) we found an optical density of 5.2 (Fig. 4.13(a)) where the fitted curve passes above the data points. This suggests that we could not detect the real absorption signal near resonance as the camera's sensitivity is limited. It cannot distinguish a "dark" shadow from a "darker" shadow. Indeed, one may observe that the top of the graph in Fig. 4.13(a) is quite flat, indicating saturation or in this case, lack of sensitivity.

# Chapter 5

# Summary

In this thesis we presented an analysis of several imaging methods applied to ultracold atom experiments. Our goal has been to understand the existing state of the art and lay the foundation for further improvements. First, we studied the theoretical basis for image formation via phase shift and absorption. Understanding the theoretical concepts of absorption, dark-ground and phase-contrast imaging methods allowed us to extract the signal and assist in increasing the SNR in our experiments.

The second stage of this work was to characterize the signal and the resolution of dark-ground and phase-contrast imaging. This preliminary stage was essential to show that these imaging systems provided a detectable phase dependent signal, and to prove that these methods are as effective as the more conventional absorption imaging in terms of resolution. As part of this work, we have also gained experience in the fabrication of thin-layered optical elements such as Fourier filters using (for the first time in cold atom imaging) ITO and chromium.

Finally, these imaging methods have been applied to ultracold atomic clouds. We analyzed the data and compared it to analytical results and numerical simulations.

This work achieved its goal in understanding and creating the state of the art cold atom imaging systems and, indeed, contributes to understand the dispersive imaging methods in non-ideal conditions where the phase dot was relatively large and the absorbance was not negligible near resonance.

In contrast to other works [Hal03, Mat99, Tur04, Ket99, Hig05], we used a low optical density object (MOT) with small diffraction pattern with respect to the

Fourier filter's size, and characterized the dark-ground and phase contrast signals using near resonance light. In these non-ideal limits we experimentally demonstrated the peculiar behavior of the dark-ground signal at the vicinity of its resonance. Moreover, we separated the absorption from the phase contrast signal under these non-ideal conditions to find information about the cloud.

One of the outcomes of this work was the creation of a new experimental and numerical algorithm to separate phase contrast data from absorption.

Based on this work, our research group will apply and improve these imaging techniques and analysis methods to the complex experimental situations which we anticipate.

# Appendix A

# Multipole expansion

The electrostatic potential of an arbitrary charge distribution $\rho(\vec{r})$ at a point R is as follows [Gri99]:

$$V(\vec{R}) = \frac{1}{4\pi\varepsilon_0}\int \frac{1}{|\vec{R}-\vec{r}|}\rho(\vec{r})\,d\tau\,, \tag{A.1}$$

where $\rho(\vec{r})\,d\tau$ is an infinitesimal charge element as illustrated in Fig. A.1.

The distance to the point of observation can be represented as:

$$|\vec{R}-\vec{r}| = \sqrt{r^2+R^2-2Rr\cos(\theta)} = r\sqrt{1+\left(\frac{r}{R}\right)\left(\frac{r}{R}-2\cos(\theta)\right)}\,. \tag{A.2}$$

The second term in the square root drops as $r/R$, which is small when the point of observation is well outside the charge distribution. Hence we can apply a binomial approximation:

$$\frac{1}{|\vec{R}-\vec{r}|} = \frac{1}{R}\left[1-\frac{1}{2}\left(\frac{r}{R}\right)\left(\frac{r}{R}-2\cos(\theta)\right)+\frac{3}{8}\left(\frac{r}{R}\right)^2\left(\frac{r}{R}-2\cos(\theta)\right)^2-\ldots\right]. \tag{A.3}$$

This expression can be written as a series of Legendre polynomials:

$$\frac{1}{|\vec{R}-\vec{r}|} = \frac{1}{R}\sum_{n=0}^{\infty}\left(\frac{r}{R}\right)^n P_n\left(\cos(\theta)\right). \tag{A.4}$$

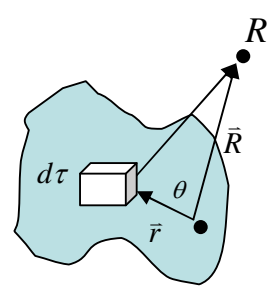


Figure A.1 – The potential of a charge distribution.

Substituting Eq. (A.4) into Eq. (A.1) results in the *multipole expansion* of the potential in the powers of $1/R$:

$$V\left(\vec{R}\right)=\frac{1}{4\pi\varepsilon_0}\sum_{n=0}^{\infty}\left(\frac{1}{R}\right)^{n+1}\int r^n P_n\left(\cos\left(\theta\right)\right)\rho\left(r\right)d\tau\,. \tag{A.5}$$

The leading order when the total charge is zero (i.e., the monopole term vanishes) is

$$V\left(\vec{R}\right)=\frac{1}{4\pi\varepsilon_0}\frac{1}{R^2}\int r\cos\left(\theta\right)\rho\left(\vec{r}\right)d\tau \tag{A.6}$$

Using a unit vector $\hat{R}$ we can simplify the above expression:

$$V\left(\vec{R}\right)=\frac{1}{4\pi\varepsilon_0}\frac{\hat{R}\cdot\vec{d}}{R^2}\,, \tag{A.7}$$

where the *dipole moment* $\vec{d}$ of the charge distribution $\rho\left(\vec{r}\right)$ is defined as

$$\vec{d}\equiv\int\vec{r}\rho\left(\vec{r}\right)d\tau\,. \tag{A.8}$$

# Appendix B

# Derivation of the polarizability

Let us expand the discussion on section 2.1.2 to find the polarizability $\alpha$. We apply $\hat{\mathcal{H}}$ to the electron wave function and use Schrödinger equation:

$$i\hbar\frac{d}{dt}\begin{pmatrix} a(t) \\ b(t) \end{pmatrix} = \hat{\mathcal{H}}\begin{pmatrix} a(t) \\ b(t) \end{pmatrix} = \begin{pmatrix} -d_{ge}b(t)E_0e^{i\omega t} + E_g a(t) \\ -d_{eg}a(t)E_0e^{-i\omega t} + E_e b(t) \end{pmatrix}. \tag{B.1}$$

Hence, we find the time derivative of the $a,b$ coefficients:

$$\begin{aligned} \dot{a}(t) &= \frac{i}{\hbar}d_{eg}b(t)E_0e^{i\omega t} - \frac{i}{\hbar}E_g a(t), \\ \dot{b}(t) &= \frac{i}{\hbar}d_{ge}a(t)E_0e^{-i\omega t} - \frac{i}{\hbar}E_e b(t). \end{aligned} \tag{B.2}$$

Let us define:

$$\begin{aligned} \tilde{a}(t) &\equiv a(t)e^{i\left(\frac{E_g t}{\hbar}\right)}, \\ \tilde{b}(t) &\equiv b(t)e^{i\left(\frac{E_e t}{\hbar}+\delta t\right)}, \end{aligned} \tag{B.3}$$

where:

$$\delta \equiv \omega - \frac{E_e - E_g}{\hbar} \equiv \omega - \omega_0. \tag{B.4}$$

Then,

$$\begin{aligned} \dot{\tilde{a}} &= \frac{i}{\hbar}d_{ge}\tilde{b}E_0 + \frac{\gamma}{2}\tilde{b}, \\ \dot{\tilde{b}} &= \frac{i}{\hbar}d_{eg}\tilde{a}E_0 + i\delta\tilde{b} - \frac{\gamma}{2}\tilde{b}, \end{aligned} \tag{B.5}$$

where the last term with γ in both equations was added to represent spontaneous emission from the excited to the ground state. When the spontaneous emission rate γ is larger than the Rabi rotation rate $dE_0/\hbar$ or when $\delta$ is large, the population of the

excited state will be always small so that to first order in $\tilde{b}$ the steady state solution (with the time derivatives set to zero) is $\tilde{a} \sim 1$ and hence:

$$\tilde{b} = -\frac{d_{eg} E_0 / \hbar}{\delta + i\gamma/2} \tilde{a} . \tag{B.6}$$

And the dipole operator can be expressed by $\tilde{a}, \tilde{b}$ :

$$\left\langle \hat{d}(t) \right\rangle = \tilde{a}^* \tilde{b} e^{-i\omega t} d_{ge} + c.c . \tag{B.7}$$

We get

$$\left\langle \hat{d}(t) \right\rangle = -e^{-i\omega t} |a|^2 \frac{d_{eg} E_0 d_{ge} / \hbar}{\delta + i\gamma/2} + c.c = -\frac{d_{eg} E(t) d_{ge} / \hbar}{\delta + i\gamma/2} + c.c . \tag{B.8}$$

It follows that the polarizability of an atom in an electric field is given by

$$\alpha = -\frac{|d_{ge}|^2}{\hbar} \frac{1}{\delta + i\gamma/2} . \tag{B.9}$$

# Appendix C

# Derivation of atom number

In order to find the atom number we shall use Eq. (2.54):

$$\phi = -\frac{\sigma_0 \tilde{n}}{2} \frac{\Delta}{1+\Delta^2}, \tag{C.1}$$

where $\Delta$ is the detuning in units of half natural linewidth and $\tilde{n} = \int n dz$ is integration of atom density along the propagation axis known as *column density* as depicted in Fig. C.1. Let us define the optical density for imaged area detected by a single pixel:

$$OD_A = \sigma_0 \tilde{n}. \tag{C.2}$$

Thus, we find the optical density per pixel as

$$OD_A = \frac{N_A \sigma_0}{A}, \tag{C.3}$$

where $A$ is the imaged area by a single pixel, $N_A$ is the total atom number in an area covered by pixel. Hence, we can find the number of atoms per imaged area by a single pixel:

$$N_A = \frac{2A}{\sigma_0} \frac{\left(1+\Delta^2\right)}{\Delta} \left|\phi_A\right|, \tag{C.4}$$

where $\left|\phi_A\right|$ is the (absolute) phase shift per imaged area in a single pixel. Hence, for the total number imaged atoms we sum over all pixels:

$$N_{\text{total}} = \frac{2A}{\sigma_0} \frac{\left(1+\Delta^2\right)}{\Delta} \sum_{Pixels} \phi_A(x, y). \tag{C.5}$$

Here we sum over all phase shifts detected in all pixels to get the total number of atoms.

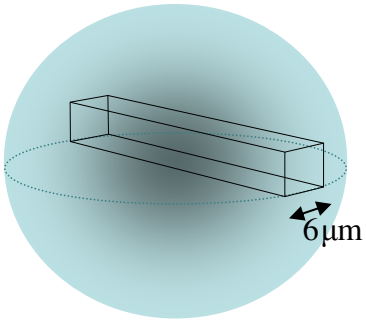


Figure C.1 - Illustration of column density in a spherical atomic cloud, for a magnification of one and a pixel size of 6µm.

# References


[And95] M. Anderson, J. Ensher, M. Matthews, C. Wieman, and E. Cornell, *Observation of Bose-Einstein condensation in a dilute atomic vapor*, Science **269**, 198 (1995).

[And97] M.R. Andrews, C.G. Townsend, H.J. Miesner, D.S. Durfee, D.M. Kurn, and W. Ketterle, *Observation of interference between two Bose condensates*, Science. vol. **275** (1997).

[Cha97] C. Champenois, E. Audouard, P. Dupla'a, and J. Vigue', *Refractive index for atomic waves: theory and detailed calculations*, J. Phys. II France **7** 523-541 (1997).

[Coh97] C. Cohen-Tannoudji in Nobel lectures, Physics text of 1997 Nobel Prize lecture.

[Dem02] W. Demtröder, *Laser spectroscopy, basic concepts and instrumentation*, 3rd ed. Springer (2002).

[Fol02] R. Folman, P. Krueger, J. Schmiedmayer, J. Denschlag, and C. Henkel, *Microscopic atom optics: from wires to an atom chip,* Advances in atomic, molecular, and optical physics, vol. **48**, 263 (2002).

[Fox06] M. Fox, *Quantum optics*, Oxford university press (2006).

[Goo96] J.W. Goodman, *Introduction to Fourier Optics*, McGraw-Hill, Boston, 2nd ed. (1996).

[Gri99] D.J. Griffiths, *Introduction to electrodynamics,* 3rd ed. Prentice-Hall (1999).

[Hal03] P.C. Haljan, *Vortices in a Bose-Einstein condensate*, Ph.D. Thesis, Univ. of Colorado, (2003).

[Hec02] E. Hecht, *Optics*, 4th ed. Addison-Wesley (2002).

[Hig05] J. M. Higbie, L. E. Sadler, S. Inouye, A. P. Chikkatur, S. R. Leslie K. L. Moore, V. Savalli, and D. M. Stamper-Kurn, *Direct, non-destructive imaging of magnetization in a spin-1 Bose gas,* Phys. Rev. Lett. **95** 050401 (2005)

[Jac98] J.D. Jackson, *Classical electrodynamics*, John Wiley & Sons. 3rd ed. (1998).

[Ket99] W. Ketterle, D.S. Durfee and D.M. Stamper-Kurn. Making, probing and understanding Bose-Einstein condensates. In M. Inguscio, S. Stringari and C. Wieman (eds.), *Bose-Einstein condensation in atomic gases: Proceedings of the International School of Physics. Enrico Fermi,*

*Varenna, Italy*. IOS Press, Amsterdam (1999), vol. Course CXL, pp. 67.176

[Ket01] W. Ketterle in Nobel Lectures, Physics text of 2001 Nobel Prize lecture.

[Lid76] D.R. Lide, *CRC Handbook of chemistry and physics*, ed. R.C. Weast: CRC Press. 57th ed. (1976).

[Lou83] R. Loudon, *The Quantum Theory of Light*, 2nd ed. Oxford, (1983).

[Lye03] J.E. Lye, *Dynamic non-destructive detection of Bose-Einstein condensates and atom lasers,* Ph.D. Thesis Australian national university. P.66 (2003).

[Mat99] M.R. Matthews, *Two-component Bose-Einstein condensation*, Ph.D. Thesis, B.S., University of Texas, 1994, Dept. of Physics (1999).

[Met03] H.J. Metcalf , P. van der Straten, *Laser Cooling and Trapping of Atoms*, Journal of the Optical Society of America B, vol. **20**, 887 (2003).

[Sal07] B.E.A. Saleh, M. C.Teich, *fundamentals of photonics,* Wiley, 2nd ed. (2007).

[Sch58] A.L. Schawlow, and C.H. Townes, *Infrared and optical masers*, Phys. Rev. **112**, 1940 (1958).

[Ste01] D.A. Steck, *Rubidium 87 D line data,* Los Alamos national laboratory (2001).

[Swa83] R. Swati, R. Banerjee, N. Basu, A.K. Batabyal, and A.K. Barua, *Properties of tin doped indium oxide thin films prepared by magnetron sputtering*, J. Appl. Phys. **54**(6), 3497 (1983).

[Tur03] D. Turner, K.P. Weber, D. Paganin, and R.E. Scholten, *Off-resonant defocus-contrast imaging of cold atoms*, Optics Letters vol. **29**, No3 (2003).

[Tur04] L.D Turner, *Holographic imaging of cold atoms*, Ph.D. Thesis, School of physics, University of Melbourne Australia (2004).

[Tur05] L.D. Turner, K.F.E.M. Domen, and R.E. Scholten, *diffraction contrast imaging of cold atoms,* Phys. Rev. A, vol. **72**, 031403 (2005).

[Zer53] F. Zernike, in Nobel Lectures, Physics text of 1953 Nobel Prize lecture.